5-2014

The Construction and Characterization of a Magneto-Optical Trap for Rubidium-87 and Electromagnetically-Induced Transparency in Rubidium-87 in a Vapor Cell

Yu Liu
University of Nevada, Las Vegas

THE CONSTRUCTION AND CHARACTERIZATION OF A MAGNETO-OPTICAL TRAP FOR RUBIDIUM-87

AND

ELECTROMAGNETICALLY-INDUCED TRANSPARENCY IN RUBIDIUM-87 IN A VAPOR CELL

By

Yu Liu

Honors Thesis submitted in partial fulfillment

for the designation of Department Honors

Department of Physics

Dr. David P. Shelton

Dr. Bernard Zygelman, Dr. Andrew Hanson

College of Sciences

University of Nevada, Las Vegas

May, 2014

Table of Contents

1. Introduction

Recent years have observed fast developments in neutral atomic vapor based quantum information storage technology. The technique utilizes light fields in the optical wavelength region as signal carrier and retriever and neutral atomic systems (e.g. single atoms, ensembles of atoms, atom-like defects in solids) as storage media. Photons are robust carriers of information due to their high velocity ($c = 2.998 \times 10^8$ m/s) and ease of transportation (they propagate rectilinearly with low loss). Their high mobility, however, makes it a challenging task to spatially localize and therefore store them. Atoms (or atom-like systems), on the other hand, can be easily localized in space while providing quantum states accessible to photons and therefore are ideal candidates for storage media. Electromagnetically-induced transparency (EIT) is a light-induced atomic coherence phenomenon that dramatically modifies the optical properties of

an atomic medium to a weak probe field by the application of a strong coupling field. As a probe pulse propagates in an EIT medium it experiences ultraslow group velocity and generates a co-propagating spin wave. These consequences of EIT can be exploited for light pulse storage and retrieval in an atomic medium.

The storage time and fidelity of information in atoms is limited by the atom-atom and atom-environment interactions which result in decoherence [1]. A further limitation on using atoms as storage media is the significant Doppler-broadening of atomic transitions at room temperature. In a room temperature atomic gas, the velocity distribution of the atoms is broad and the Doppler shifts in the atomic energy levels means that photons of a given frequency are only in resonance with atoms belonging to a narrow velocity group [2]. A cold ($T << 1$ k) atomic sample, on the other hand, is a superior form of storage medium due both to its weak internal and external interactions (which leads to increased coherence lifetime) and its narrow velocity distribution (which means nearly all the atoms in the sample are in resonance with the light field). Alkali atoms can be cooled to subKelvin temperatures through optical cooling, a technique first demonstrated by Wineland *et al*. in 1978 [3]. After being cooled the atoms can be trapped using a magneto-optical trap, creating a standing cloud of trapped atoms.

EIT-based light storage has been demonstrated and investigated experimentally for both classical light pulses as well as single photons using both warm atomic vapor and cold atoms. The aim of this study is create a setup capable of light storage in cold rubidium (Rb) atoms. In this thesis we will describe the setup we have constructed for optically cooling and trapping and present results on the characterization of various trap parameters (e.g., size, population, temperature). We will also present our study on EIT in a warm vapor cell, setting up the stage for studying EIT and slow light in cold atoms. Our setup and results provide the basis for studying

EIT in cold atoms and eventually towards the coherent light storage and retrieval in cold atoms using EIT.

2. Theoretical Background

2.1. Extended Cavity Diode Lasers (ECDLs): construction and stabilization

Lasers can produce intense, coherent light fields suitable for optical cooling and optical probing techniques required for the study. To understand the choice of using semiconductor diode lasers as the light source we must briefly discuss the energy structure of Rb atoms.

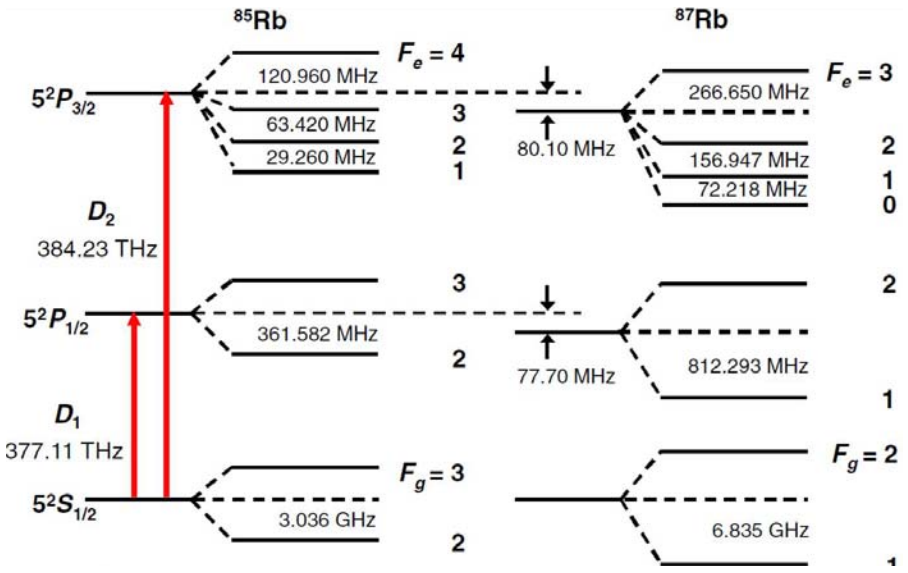

Figure 1 Predicted Energy Structures for ^{85}Rb and ^{87}Rb [6]

Rb has two naturally occurring isotopes: ^{85}Rb (72% abundant) and ^{87}Rb (28% abundant). The ground state electronic structure of Rb (Z=37) can be approximated as a single 5s valence electron outside of the closed shell of Kr ($1s^2 2s^2 2p^6 3s^2 3p^6 4s^2 4p^6$). Only the valence electron

participates in transitions in the optical regime. The prominent Rb D_2 transition occurs between the $5S_{1/2}$ and $5P_{3/2}$ energy levels at a wavelength of 780.0268 nm for both isotopes. Due to spin-spin interactions between the electron and the nucleus, each of the energy levels is further split into hyperfine levels illustrated in Figure 1 [6].

As we will illustrate in subsequent sections, in order to perform optical cooling and EIT it is important that the laser is able to access each allowed transition (indicated by an arrow in Figure 1). Therefore our experiments require laser sources that lase at ~780 nm and are continuously tunable over a frequency range of > 8 GHz (the largest splitting is 6.83 GHz and occurs between the $5S_{1/2}$ F=1 and F=2 energy levels in ^{87}Rb). Extended cavity diode lasers (ECDLs) fulfill our requirements well. A laser diode is a semiconductor chip that radiates by passing a current through its *p*-*n* junction and inducing electron-hole recombination processes. An optical cavity is formed by the front and back facets of the diode chip, allowing laser action to occur even in a solitary diode. In an ECDL the laser diode is placed inside a much longer external optical cavity formed by the back facet of the diode chip and a rotatable external grating, providing tunability in the laser frequency. Our ECDL design follows that developed by Arnold *et al*. (1997) [7]. The schematic is given in Figure 2. The design features a laser diode, a collimating lens, and a piezoelectric transducer (PZT) driven, blazed grating. The first order diffracted beam from the grating is directed back to the laser to act as an optical feedback signal. Changing the grating angle therefore results in change in the laser frequency, achieving tunability. We have constructed two new ECDL modules in addition to two existing ones, making a total of four lasers to function as the cooling and repump lasers for trapping, as well as the probe and coupling lasers for studying EIT, respectively.

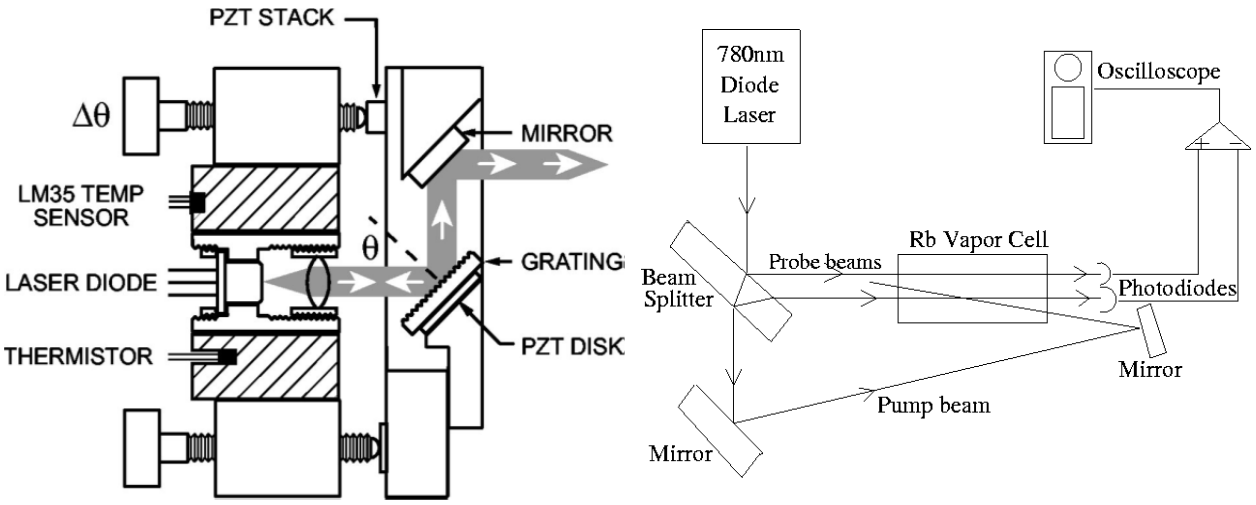

Figure 3 [7] a. the schematic of an ECDL with grating feedback; b. Optical setup for saturated absorption atomic reference

Optical cooling and certain optical probing techniques require each laser to be stable within hundreds of kilohertz about a single frequency. The frequency of a diode laser is affected by factors including but not limited to temperature, pressure, mechanical vibrations, and uncontrolled optical feedbacks (e.g. from backscattered light). In addition to minimizing the effect from these factors, the lasers need to be frequency locked, in our case specifically, to the Rb transitions. The generic servo circuit used to lock the laser is depicted in a simple block diagram in Figure 3. Saturated absorption is a standard technique to obtain a Doppler-free reference spectrum that contains the hyperfine transition features that we wish to lock onto. The optical setup for producing a saturated absorption signal is shown in Figure 2b.[2] It is described

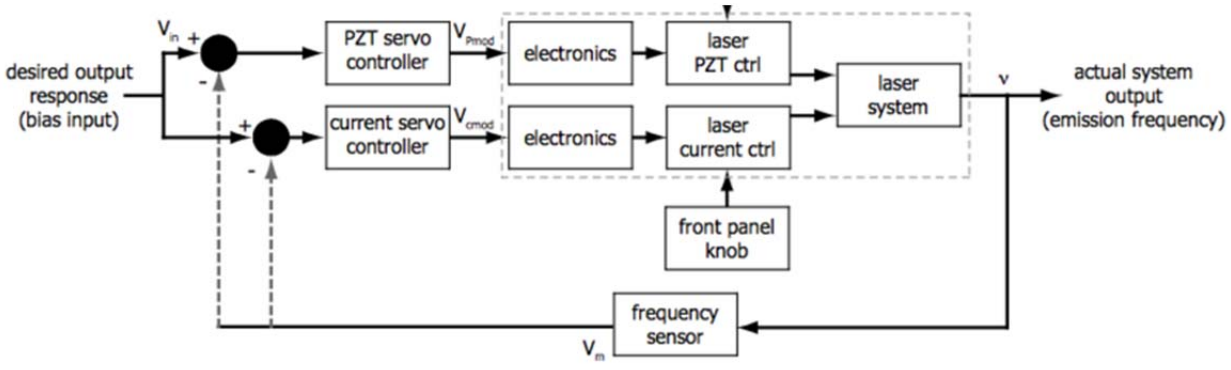

Figure 2 Box diagram for laser frequency locking

in detail in section 3.2.

2.2. Optical Cooling and Trapping of Rb Atoms

Optical cooling is the process of slowing down neutral atoms or ions using radiation scattering force from quasi-resonant laser beams. Since the temperature of a group of particles is proportional to the square of their average velocity, slow implies cold. This idea was first proposed by Wineland and Dehmelt (1975) [9] and first experimentally demonstrated by Wineland *et al* (1987) where they cooled a cloud of Mg^+ ions held in a Penning trap [3].

The strength of interaction between light and atoms is a strong function of the frequency of the light. When the light frequency approaches the frequency of an atomic transition, the resonant condition is satisfied and the light-atom interaction is greatly enhanced. In the resonant case, light is strongly absorbed as it propagates through an atomic medium. Suppose that a stream of atoms traveling in a certain direction with resonant transition frequency ω_0 is incident upon by a counterpropagating laser beam (which can be pictured as a stream of photons) with frequency ω_L. Each absorbed photon transfers its momentum to the atom in the direction of its travel whereas the emitted photons go off in random directions. The overall effect is a force from the laser beam that slows the atoms down, known as the scattering force. The magnitude of the force in the direction of the laser beam is given by

Equation 1

$$F_{scattering} = (\text{photon momentum}) \times (\text{scattering rate})$$

$$= \hbar k \frac{1}{2\tau}\left(\frac{2I/I_s}{1 + 2I/I_s + 4(\omega_L - \omega_0 + kv)^2\tau^2}\right),$$

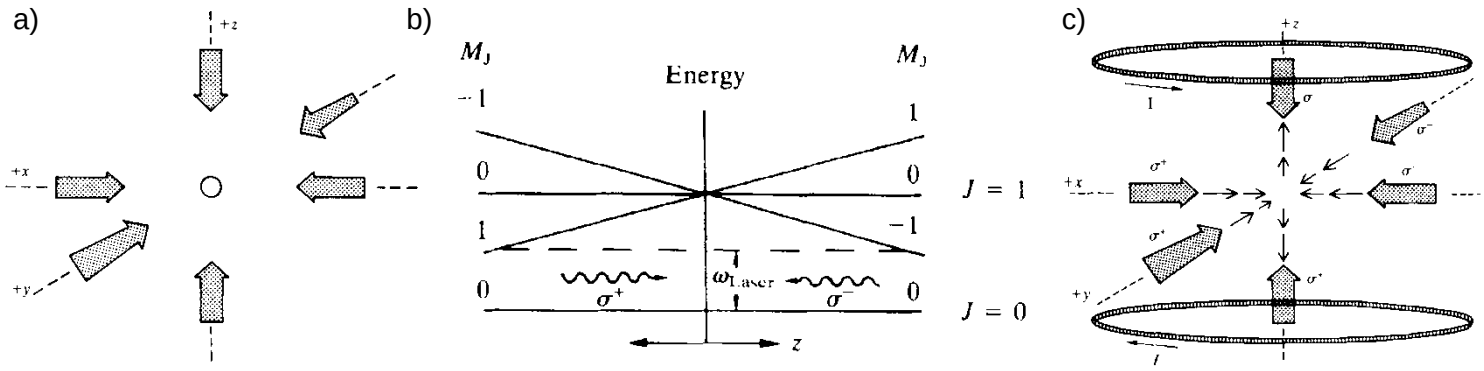

Figure 4 a. Optical molasses; b. Spatial-dependent Zeeman energy splitting and circularly polarized laser beams leading to optical trapping; c. Schematic for a magneto-optical trap (MOT)

where k is the wave vector of the laser, τ is the lifetime of the excited state, I is the intensity of the laser and I_s is the saturation intensity for the atomic transition [10]. Notice that because the atoms are travelling with respect to the photons, the frequency of the photons observed in the atom's rest frame is Doppler-shifted by the amount kv, where v is the velocity of the atom. This means the maximum scattering force is obtained at resonant condition $kv = \omega_0 - \omega_L$. The Doppler-shift dependence of the scattering force is why this cooling mechanism is also known as Doppler cooling [11].

The idea of Doppler cooling is naturally extended to three dimensions, giving rise to *optical molasses*. Suppose the atoms are situated inside the intersection of three pairs of counterpropagating beams (derived from the same laser, which we call the *cooling laser*) along the Cartesian axes, as depicted in Figure 4a. Stationary atoms ($v = 0$ m/s) will receive no net force since the radiation forces from all six directions balance each other out. Atoms moving in any direction will experience an imbalance in the forces caused by the Doppler effect and receive a net force directed oppositely to its travel. The overall effect is that in the intersection region the light exerts a damping force on the atoms, much like the damping effect of a viscous fluid on the

particles that move through it. Thus this cooling configuration became to be known as optical molasses. [10]

An optical trap is formed by adding a quadrupole magnetic field that is zero at the center of the intersection and varies linearly with the distance away from the center. The field can be produced by an anti-Helmholtz coil consisting of two coils with opposite currents (see Figure 4c). To understand the mechanism of magnetic trapping, consider an ideal two-level atom with ground state $J = 0$ and excited state $J' = 1$. The spatially varying magnetic field causes a spatial variation in the magnetic sublevels due to Zeeman splitting, as depicted in Figure 4b. This leads to an imbalance in the radiation forces if each pair of cooling beams is circularly polarized with the opposite handedness (represented by σ_+ and σ_- in Figure 4b and 4c, respectively) and red detuned ($\omega_L < \omega_0$) with respect to the resonant frequency of the atoms near the center of the trap. The overall effect is a radially increasing radiation force that pushes all the cooled atoms with sufficiently low kinetic energy towards the center of the trap, where the field is zero. [10] This configuration, known as the Magneto-optical trap (MOT) and first demonstrated by Raab *et al*. in 1987, is ideal for preparing a spatially localized, optically dense cloud of cold atoms [12].

Now consider the specific case of trapping Rb atoms. A commonly used cooling transition in ^{87}Rb is the $F = 2 \rightarrow F' = 3$ transition. In light of our discussion on the cooling of an ideal two-level atom with no Zeeman splitting in the ground state and a threefold splitting in the excited state, the $F = 2 \rightarrow F' = 3$ transition, with a fivefold splitting in the $F = 2$ level and sevenfold in the $F' = 3$ level, can be pictured as consisting of five sets of the simple two-level system. Unfortunately about 1 in every 1000 photons emitted from the $F' = 3$ state falls to the $F = 1$ ground state and therefore becomes inaccessible to the cooling laser [11]. In order to keep the electrons in the cooling cycle, a second laser beam tuned to the resonant frequency between

the $F = 1$ and any F' states is required to "repump" the electrons back into the cycle. Hence this laser is oftentimes called the *repump laser*. Due to the similarity in atomic structures between the two isotopes of Rb, ^{85}Rb can be trapped equally well using the corresponding cooling and repump transitions. With the large tuning range of the ECDLs provided by the grating feedbacks, we can in theory trap either of the two isotopes. Trapping a reasonable number (10^6) of atoms requires ~5mW of cooling power and ~1mW of repump power, which are readily provided by ECDLs.

Once produced, the cold Rb atoms can be easily observed using an near-infrared-sensitive CCD camera as a bright cloud appearing at the center of the trap (zero-field point) that is easily distinguished from the fluorescence due to untrapped background atoms. The absorption spectrum obtained from the cold atoms should be essentially free of Doppler-broadening; the linewidths of the absorption peaks therefore is expected to be close to the natural linewidth. The full width at half maximum (FWHM) Doppler-broadening of an atomic absorption line as a function of temperature T is given by

Equation 2

$$\Delta\nu(T) = \nu_0 \frac{\langle v \rangle}{c} = \frac{\nu_0}{c}\sqrt{\frac{8kT\ln 2}{m}}$$

Thus the Doppler width of the absorption lines contains information on the mean velocity of the atoms and therefore the temperature of the cloud. However, typical temperatures obtained in a MOT are of the order 100 μK [14], corresponding to $\Delta\nu$~0.3 MHz, which is a small fraction of the natural linewidth and therefore difficult to accurately detect, especially in the presence of

finite laser linewidth. More deterministic ways of assessing the trap temperature are discussed in the following section.

2.3. Characterization of the MOT

In characterizing the MOT we are interested in measuring three key parameters: the number of trapped atoms, the size of the atom cloud, and the temperature of the atom cloud [11]. The number density of the cloud can be easily calculated from the previous two quantities. In this section we describe the methods and equipment used for measuring each parameter.

The number of atoms in the trap can be estimated from the intensity of the fluorescent light emitted by the atom cloud as they are excited by the cooling beam. In the case of isotropic light polarization, as is in the case of a MOT, the rate R at which a single atom in the cloud scatters photons is given by (values in parentheses are given for the ^{87}Rb $F = 2 \rightarrow F' = 3$ transition) [11]:

Equation 3

$$R = \frac{(I/I_s)2\Gamma}{1 + I/I_s + 4(\Delta/\Gamma)^2},$$

where I is the sum of intensities of the three pairs of cooling beams, I_s ($= 3.577\ \mathrm{mW/cm^2}$) is the saturation intensity for the given transition, Γ ($= 6\ \mathrm{MHz}$) is the natural linewidth of the transition. and Δ is the detuning of the laser frequency from resonance. A typical number for R is $6 \times 10^6\ \mathrm{photons/(s \cdot atom)}$. Using a calibrated photodiode to collect fluorescent light at a known detection solid angle, one can calculate the amount of trapped atoms. We can establish

the following relationship between the photon scattering rate and the photocurrent generated in the photodiode:

$$\text{Number of atoms} \times \text{single atom scattering rate} \times \text{fraction of photons collected by the lens} \times \text{photodiode quantum efficiency} = \frac{\text{Photocurrent}}{\text{charge per carrier}},$$

or

$$N_p \times R \times \frac{d\Omega}{4\pi} \times \eta_{PD} = \frac{i}{e}.$$

Therefore the number of atoms in the MOT is given by

$$N_p = \frac{8\pi[1 + (\Delta/\Gamma)^2 + I_0/I_s]}{\Gamma(I_0/I_s)\eta_{PD}d\Omega}\frac{i}{e},$$

where the detection solid angle for a lens of clear aperture D and image distance d_0 is given by

$$d\Omega = \frac{\pi(D/2)^2}{d_0}.$$

Wieman *et al*. estimated that nearly 4×10^7 trapped atoms were obtained with 7 mW from the cooling laser [11]. One can make an estimate of the size of the cloud by imaging the cloud using a near-infrared-sensitive CCD camera and displaying the image on a video monitor with calibrated scales. A more sophisticated method to measure the size of the cloud is by absorption imaging, described in detail in reference [13].

The temperature of the trapped atoms is measured by time-of-flight (TOF) or release and recapture (R&R) methods. Both methods require the trapped atoms to be released by turning off the cooling beam and/or the trapping magnetic field. The typical course of a TOF experiment is

on the order of a few to a few tens of milliseconds, which requires the beam and/or the coil to be shut off in a time period ≤ 1ms [14]. The coil can be shut off on a sub-millisecond time scale by using a bipolar transistor switch to cut off the driving current, while the beam can either be shut off in several milliseconds using a light chopper or in a few microseconds using an electro-optical modulator, a device we will introduce in section 2.5 when we discuss slow light experiments where microsecond timing becomes important.

In a typical TOF experiment, a probe beam (from a separate third laser) is placed below the trapped cloud (Figure 5a) [14]. Once the cloud is released, it drops under the influence of gravity while expanding ballistically. As the atoms pass through the probe beam, two processes occur: they absorb photons from the probe beam and re-emit them through fluorescence. Thus a TOF signal can be obtained by monitoring either the probe intensity or the fluorescence intensity as the atoms transit through. The variation of the TOF signal as a function of time can be read on an oscilloscope and the flight time is the time difference between trap off and signal peak. Brzozowski *et al*. (2002) modeled the TOF process based on a falling and expanding sphere, allowing one to calculate the trap temperature from the flight time [15]. Their model was in good agreement with their experimental TOF signals for short probe-to-trap distances. Our TOF experimental setup will follow that by Lett *et al*. (1988) [14]. Their experiment was carried out on sodium atoms in an optical molasses with a probe-to-molasses distance of 1.1 cm and a cooling laser detuning of 20 MHz. Figure 5b shows the TOF signals obtained for two different trap temperatures. As one expects, a shorter flight time is obtained for a higher trap temperature. The shape of the signal reflects the distribution of velocities in the sample. In our proposed optical setup, laser #2 is designated to be the probe laser.

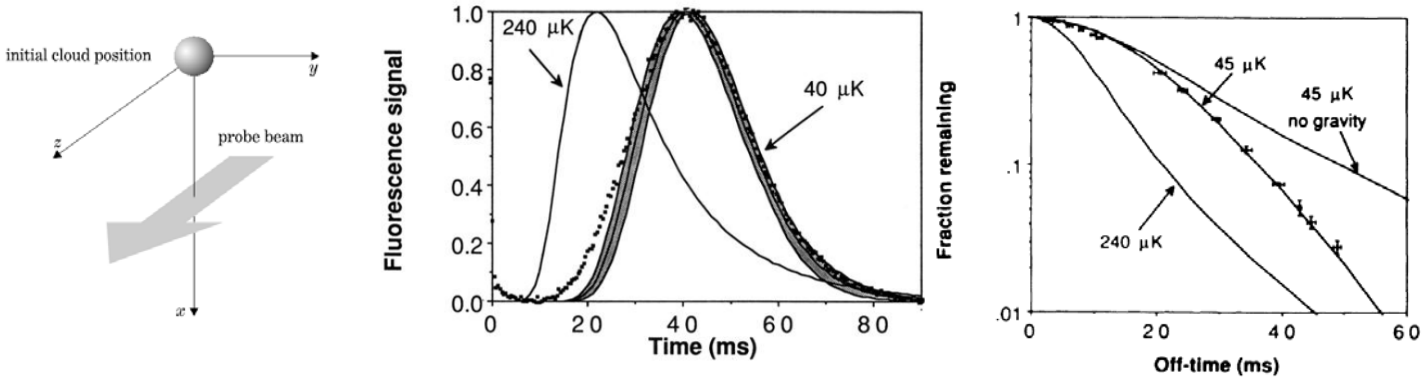

Figure 5 [14][15] a. Schematic for a TOF measurement setup; b. Variation of the fluoresence signal as a function of time for a typical TOF measurement; c. Variation of the atoms remaining in the trap as a function of trap off-time in a typical R&R experiment.

In an R&R experiment, the cooling beam is turned off for a short period of time t_{off} and then turned back on. The atoms that did not have enough time to escape the intersection region fluoresce as the cooling beam turns back on. By measuring this fluorescence as a fraction of the total fluorescence when the trap is fully filled one obtains the fraction of atoms still remaining in the intersection. The fraction of atoms remaining decreases as a function of t_{off}. For a given t_{off}, the higher the trap temperature, the less fraction remaining there is. This is reflected in Figure 5c, which shows the result of R&R experiments carried out by Lett *et al*. (1988) [14].

Our experimental setup is modeled after the design by Wieman and Flowers (1994) [11]. They have developed an inexpensive set of apparatus suitable for undergraduate laboratories.

2.4. Electromagnetically-Induced Transparency

Electromagnetically induced transparency (EIT) in atomic systems is a quantum interference effect resulting in reduced absorption of a weak probe field propagating through an otherwise opaque atomic medium in the presence of a strong coupling field [16]. In order to establish EIT, the probe and coupling fields, of frequency ω_p and ω_c respectively, must be quasi-

resonant with two atomic transitions that share a common state and are linked by a dipole forbidden transition. Figure 6 shows the three types of EIT systems, commonly referred to as the ladder (a), Λ (b), and V (c) types, respectively. We follow the convention used by Olson and Mayer (2008) and refer to the common state $|2\rangle$ and the two states linked by the dipole forbidden transition $|1\rangle$ and $|3\rangle$, respectively [17]. In light of the application of EIT in quantum information storage, the probe field is also known as the signal field and the coupling the control (Figure 6d) [5]. Since EIT is inherently a quantum interference effect, understanding the physics of EIT requires a quantum mechanical treatment. We provide a brief quantum mechanical treatment of an ideal three-level EIT system in Appendix III; here we shall focus on the important results from the treatment.

In the Λ-type system depicted in Figure 6b, for example, the weak probe laser beam is resonant with the $|1\rangle \rightarrow |2\rangle$ transition of an atomic medium where the strong coupling laser the $|3\rangle \rightarrow |2\rangle$ transition. The $|1\rangle \rightarrow |3\rangle$ transition is dipole forbidden. In the absence of the coupling laser, the probe laser is naturally absorbed by the medium. In this case the variation of the absorption (or optical density) and dispersion (or index of refraction) of the medium to the probe laser as functions of the detuning Δ_p (Figure 6c) is given by the red curves in Figure 14a and 14b

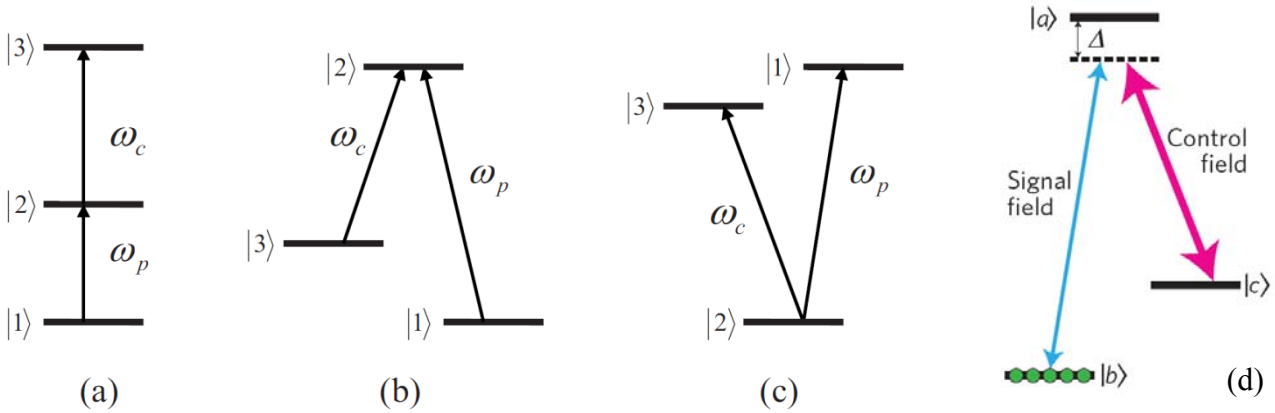

Figure 6 [17][5] a, b, and c. three different types of EIT systems; d. A Λ-type system used for quantum information storage

[5]. Absorption and dispersion are two intimately related phenomena. A quantitative treatment of their relationship is given in Appendix III. The real part of the linear susceptibility $\chi(\omega)$ of a medium gives the refractive index $n(\omega)$ where the imaginary part gives the absorption coefficient $\alpha(\omega)$. Qualitatively speaking, the sharper the absorption profile, the stronger the dispersion is (i.e. $dn/d\omega_p$ is large). In the presence of the coupling laser, however, the atoms in the medium can now absorb through either the $|1\rangle \rightarrow |2\rangle$ transition or the $|1\rangle \rightarrow |3\rangle$ transition. The two possible quantum pathways can interfere destructively with each other, leading to no absorption at all. The atoms in this case are said to be in the "dark states." Thus the medium becomes *transparent* to the probe laser. This results in dramatic modifications to the absorptive and dispersive properties of the medium to the probe laser, given by the blue curves in Figure 7a and 7b. The coupling laser induces a narrow transparency window in the absorption profile of the probe laser. The width of the window is proportional to the intensity of the coupling laser. The resulting dispersion curve features a steep portion with a positive slope near resonance ($\Delta = 0$ MHz) that was absent on the red curve. This will become significant when we discuss the reduced group velocity of a probe laser pulse as it propagates through an EIT medium.

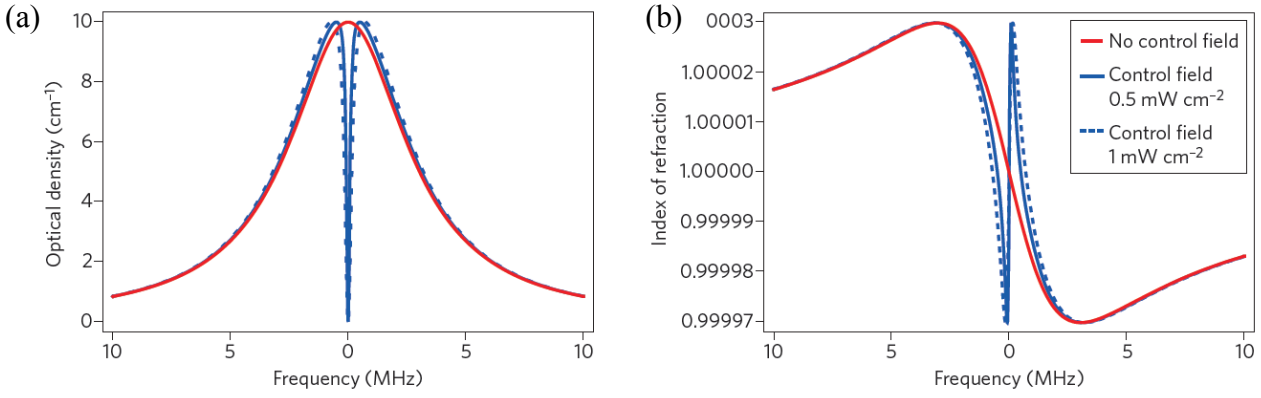

Figure 7 [5] a. The absorption spectrum of the probe beam under EIT conditions; b. The dispersion spectrum of the probe beam under EIT conditions.

The first experimental demonstration of EIT was carried out by Boller *et al.* in 1991, in which the term was coined [4]. Using a Λ-type system in a vapor of strontium ions and a 1mW coupling field, they successfully increased the transmission of a probe beam through the medium from e^{-20} to e^{-1}. EIT in Rb atoms has been studied extensively over the past two decades [16-19]. In particular, Tiwari *et al*. (2010) has studied EIT in cold ^{85}Rb atoms trapped in the $F = 2$ hyperfine ground state [16]. Their experimental setup (Figure 8a) features linearly polarized probe and control beams passing through a cloud of cold ^{85}Rb atoms at a 90 degree angle. The cooling, repump, coupling, and probe transitions are shown in Figure 8b. Incidentally, the repump and control transitions are of the same frequency and therefore a single laser beam is used for both purposes. The energy levels involved form a Λ-type EIT system, with $F = 3$ and $F = 2$ as the ground states and $F' = 2$ as the common excited state. Due to hyperfine structure, each energy level is split into $2n + 1$ magnetic hyperfine levels that are degenerate at zero magnetic field (Figure 8c). This particular EIT system is *complete* in the sense that every transition between an $F = 2$ sublevel and an $F' = 3$ sublevel is able to interfere with a transition between an $F = 3$ sublevel and an $F' = 3$ sublevel. Thus the simple three-level EIT system (Figure 8c, left) can be pictured as the superposition of several equivalent, simultaneously driven EIT systems (Figure 8c, right), provided that the zero-field condition holds reasonably well (in this study the spatial variation of the magnetic field across the cloud is ~1G). The probe frequency is scanned from -40 MHz to +40 MHz about the $F = 3 \rightarrow F' = 2$ resonance and probe transmission is monitored by a photodiode (PD-1 in Figure 8a). The result is shown is Figure 8d. The probe transmission profile is a normal Lorentzian absorption profile with an EIT transparency window (peak) at the center. The data are in good agreement with the theoretical prediction (Figure 8e).

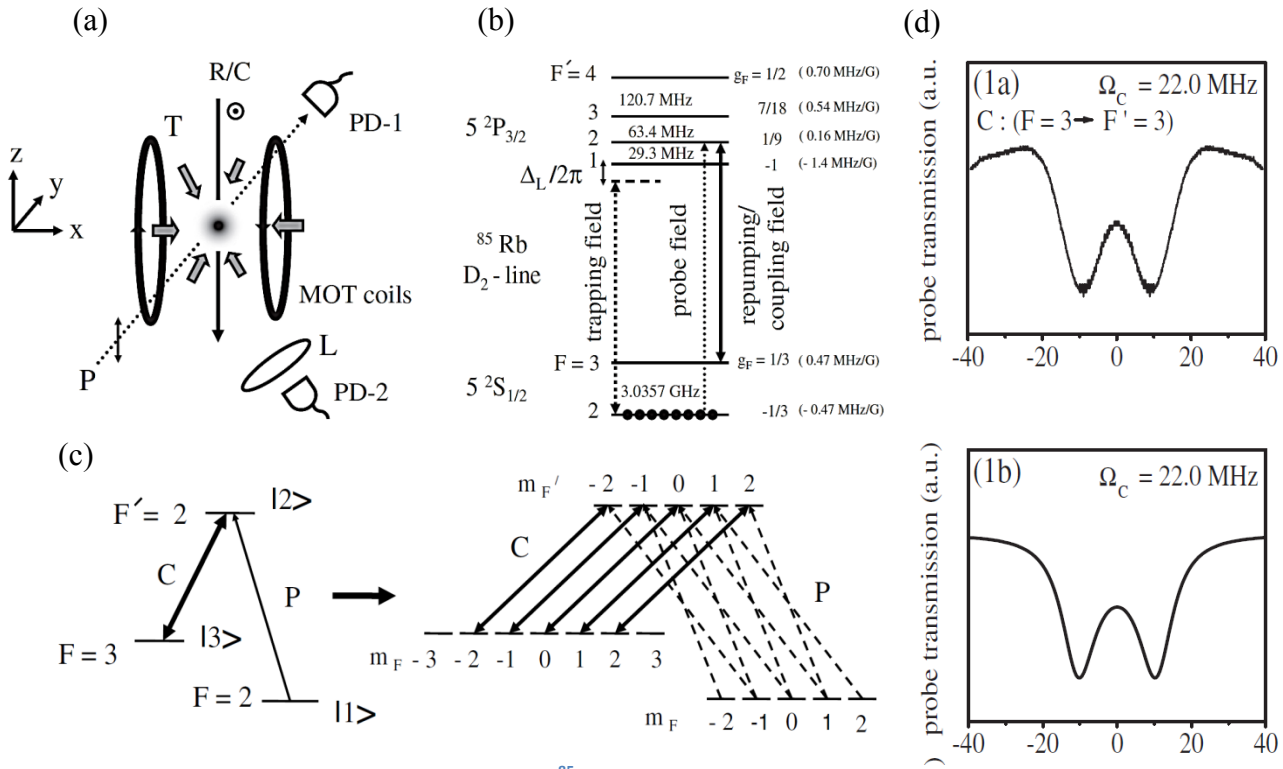

Figure 8 [16] A summary of the EIT experiment on cold ^{85}Rb atoms performed by Tiwari et al. a. The optical setup; b. The energy level diagram of ^{85}Rb with relevant transitions labeled; c. the EIT system studied and its decomposition to Zeeman components; d. the resulting EIT absorption spectrum and theoretically predicted curve for comparison.

The particular EIT system in the above study provides a potentially useful basis for our study of slow light and quantum information storage. Other EIT systems in Rb have been studied [17-19]. With the tunability of ECDLs, we have the freedom to choose one or more of the available EIT systems as the basis for our subsequent investigations. Our optical setup follows that described in Figure 8a, where the probe and coupling lasers are arranged orthogonally to ensure that the EIT signals are produced only by the cold atoms, not the background atoms. As we scan the probe laser frequency about an atomic resonance of the cold atoms while the coupling beam is locked onto the center of that resonance, we are expecting to observe an EIT transparency window at the center of a normal absorption spectrum. The transparency window is determined by the transmission of the probe through the medium as a function of its detuning $T(\omega)$. Near resonance, the shape of the transparency window is approximated by

Equation 4

$$T(\omega_p) \approx \mathrm{Exp}[-(\Delta/\Delta\nu)^2],$$

where the characteristic width of the window is given by

$$\Delta\nu = \sqrt{\frac{c}{\gamma_{31}L}\frac{|\Omega|^4}{g^2N}}$$

where γ_{31} is the decoherence rate of the $|1\rangle \rightarrow |3\rangle$ transition, L is the length of the medium, g is the atom-field coupling constant that describes the strength of the interaction (Appendix III), N is the number of atoms in the medium, and Ω is the Rabi frequency of the coupling beam and is proportional to the square root of the beam intensity (Appendix III). From the above expression one notices that the transparency window decreases as the decoherence rate, length of the medium, or the atomic density increases, and increases as the coupling beam intensity increases. These variations lead to experimental considerations for storing a light pulse in an EIT medium, as discussed in the previous section.

2.5. EIT-Based Slow Light and Light Storage

In addition to induced transparency, another striking observation from EIT is the dramatic reduction in the propagation velocity of a pulsed probe beam [5]. To understand the physics of slow light, consider light of frequency ω traveling through a dispersive medium (i.e. the refractive index of the medium n is a function of ω). In continuous wave mode, light travels through the medium at the phase velocity given by $v_p = n/\omega$. In pulsed mode, however, the light pulse travels at the group velocity v_g given by $1/v_g = \partial k/\partial\omega = k_0[\partial n_g(\omega)/\partial\omega]$, where

k_0 is the vacuum wavenumber of the light pulse and it is related to the vacuum wavelength by $k_0 = 2\pi/\lambda_0$. The group index of refraction n_g is related to normal index of refraction n by $n_g(\omega) = n(\omega) + \omega[\partial n(\omega)/\partial\omega]$. Thus the group velocity is given by the expression [20]:

Equation 5

$$v_g = \frac{c}{n(\omega) + \omega[\partial n(\omega)/\partial\omega]} .$$

From the expression one notices that as $\partial n/\partial\omega$ becomes large, v_g becomes small. For regular transparent materials such as glass, $\omega[\partial n(\omega)/\partial\omega] \ll n$ and v_g tends to the phase velocity v_p and therefore no significant slowing effect is observed. But in an EIT material near resonance one can have $\omega[\partial n(\omega)/\partial\omega] \gg n$. In Figure 14b, for example, the slope of the dispersion curve near resonance is $\partial n(\omega)/\partial\omega \approx 4.8 \times 10^{-10}$ Hz^{-1}. Thus for the Rb 780 nm transition for which $\omega = 2.4 \times 10^{15}$ Hz, $\omega[\partial n(\omega)/\partial\omega] \approx 10^6 \gg n(\omega) \approx 1$. This means the group velocity v_g is, in this particular example, a mere 300 m/s, approximately one millionth of the vacuum speed of light c. Accompanying the slowing is the spatial compression of the light pulse. A light pulse of duration, for example, 10 μs in vacuum correspond to a spatial extent of 3 km. In the EIT medium discussed above, the same pulse will be compressed by the ratio c/v_g and have a 3 mm spatial extent, short enough to fit into the cold atom cloud we can generate in a MOT. It is natural to express v_g in terms of parameters of the medium and the coupling beam. Since $n = 1 + 1/2\,\mathrm{Re}[\ \chi(\omega)\ ]$, we have from Equation 5

Equation 6

$$v_g = \frac{c}{1 + g^2 N/|\Omega|^2} \approx \frac{c|\Omega|^2}{g^2 N}.$$

Therefore the delay τ of the pulse in a medium of length L is given by

Equation 7

$$\tau = \frac{L}{v_g} - \frac{L}{c} = \frac{L}{c}\frac{g^2 N}{|\Omega|^2} \ ,$$

which means decreasing the coupling power or increasing the atomic density increases the delay.

The slowdown and spatial compression effects of EIT provide the basis for light storage [5]. Consider the EIT light storage schematic depicted in Figure 9a and suppose the system is the one given in Figure 6d. The control field (red) is initially on before the arrival of the signal pulse (blue wiggles), making the medium appear transparent to the signal pulse. As the signal just fits entirely into the length of the medium, the control field is adiabatically turned off, rendering the medium opaque to the signal pulse such that it is trapped inside the medium. When the pulse needs to be retrieved, the control field is adiabatically turned back on, restoring the transparency condition and the probe pulse resumes its propagation. The interaction between the light pulse and the atoms during the storage process is most accurately described by the dark-state polariton formulation described in detail in ref [23] and summarized in Appendix II. The physical picture is the following. The hyperfine ground states of an alkali atom (e.g. Rb) are split according to the

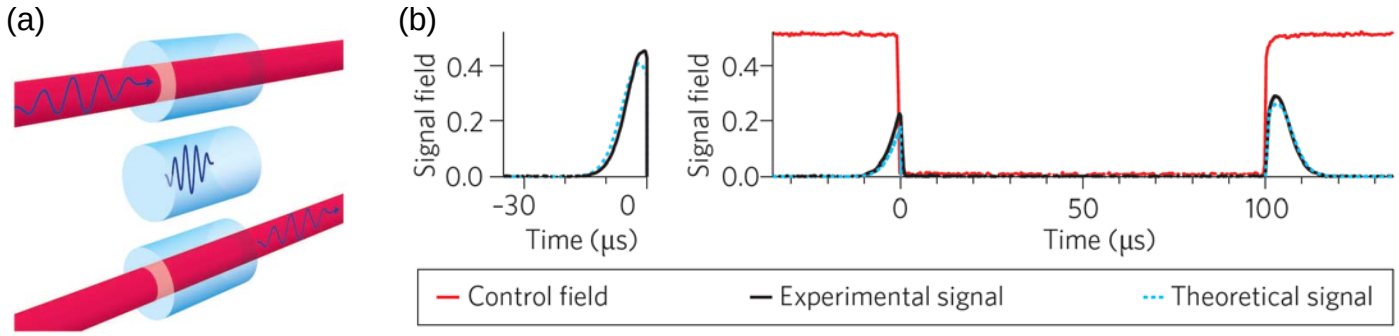

Figure 9 [5] a. Schematic illustrating the storage and retrieval processes of a pulse of light in an EIT medium; b. the time courses of the control beam and signal pulse corresponding to the experiment illustrated in a.

spin state of the valance electron. Thus for an atom to evolve from one ground state into the other, a spin flip is involved. Consider a Λ-type EIT system (Figure 6d) in an alkali atom (e.g. Figure 8c). As we have discussed in Appendix III, under EIT condition an atom exists in a coherent superposition of states $|b\rangle$ and $|c\rangle$, which is translated into the superposition of the spin state of the electron. In the dynamic situation depicted in Figure 16a, virtually all the atoms initially exist in state $|c\rangle$ due to optical pumping from the strong control field. As the probe pulse propagates through the medium, coherence between $|b\rangle$ and $|c\rangle$ is established. In other words, atoms in spatial overlap with signal pulse are driven into state $|b\rangle$, undergoing a spin flip in the process. As the signal pulse propagates through the atoms out of overlap with the pulse will be driven back into state $|b\rangle$. Thus a "spin wave" co-propagating with the light pulse is generated inside the medium, as depicted in the schematic in Figure 10[23]. The dark-state polariton $\Psi(z,t)$ is essentially a quantity characterizing the relative amplitude of the light wave $E(z,t)$ and the spin wave $s(z,t)$ as the probe pulse propagates through the medium. When the coupling field is on the polariton is purely photonic, i.e. the probe pulse propagates; where when the coupling field is off it is purely atomic, i.e. the probe pulse is stored in the collective spin excitation of the medium.

There are two practical issues to concern when storing a light pulse in an atomic medium. Firstly, the decoherence rate between the two different ground states γ_{13} is always finite. Which

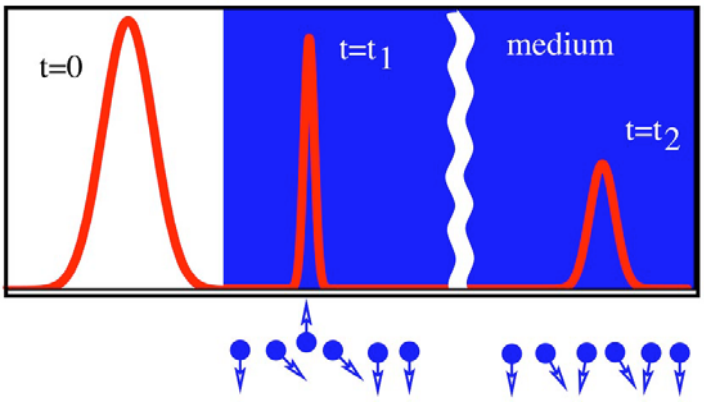

Figure 10 The schematic time course of the probe pulse and (red curves) the corresponding spin wave (blue dots) as the pulse propagates in an EIT medium.

means after a characteristic time $\tau_{13} = {\gamma_{13}}^{-1}$ the atom will drop into either ground state and will no longer contribute the spin wave and therefore the storage. Secondly, in order to preserve the shape and spectrum of the probe pulse, the spectral bandwidth of the pulse must fit into the transparency window during its propagation inside the medium. The part of the probe spectrum that falls outside the window will be absorbed by the medium. In the continuous wave case of EIT discussed in section 2. 4, the bandwidth of the probe probe beam is only limited by the performance of the laser. In the pulsed case, however, the bandwidth of the probe pulse is the inverse of its time duration T. Equation 4 shows that the transparency window width decreases with increasing propagation distance and atomic density. This means there must be $1/T < \Delta\nu$, which means we have (from Equation 4 and 7) an upper limit on the ratio between the pulse delay and pulse duration

$$\frac{\tau}{T} < \sqrt{\frac{g^2 NL}{c\,\gamma_{31}}}\,.$$

In order for a pulse to be completely stored inside a medium of length L, the delay must be much larger than the duration of the pulse. Therefore we require

$$\sqrt{\frac{g^2 NL}{c\,\gamma_{31}}} \gg 1\,,$$

which means an optically dense medium and/or low decoherence rate between the ground states $|1\rangle$ and $|3\rangle$.

For both the above reasons, a high decoherence rate γ_{13} is detrimental to the preservation of the probe pulse in the storage process. The atomic decoherence scales up as the phase

instability between the coupling and probe lasers, defined as the variance of the relative phase between the two $\langle\varphi^2\rangle$. Therefore a digital phase lock following the design in ref [8] will be constructed and used to maintain the phase stability between the two lasers. Höckel *et al.* used a similar digital phase lock for their EIT experiments in a warm cesium vapor cell. For a phase stability of $\langle\varphi^2\rangle < 0.02\ \mathrm{rad}^2$, they were able to obtain a reasonable decoherence rate of ~110 kHz , a peak transparency of >60%, and an EIT window of width 1.1 MHz at an optical depth of ~400 [24].

Phillips *et al*. performed EIT-based light storage experiments on warm Rb atoms in a buffer gas-filled vapor cell [21]. The control and signal intensities are monitored by two separate photodiodes. The time courses of the signal pulse and the coupling field from their work are shown in Figure 16b. The signal pulse is prepared as shown on the left hand side. At $t = 0$ μs, the control beam is turned off and the majority of the signal pulse is trapped in the vapor cell (The tail from $t = -10$ μs to $t = 0$ μs represents the portion of the probe pulse that escaped the cell before the control beam is turned off). At $t = 100$ μs, the control field is turned back on, allowing the trapped signal pulse to resume propagation. For storage time of 100 μs, the stored probe pulse is recovered with negligible energy loss. Light storage time (storage time corresponding to an e-fold reduction in the probe energy before and after storage) as long as 16s in an ultracold Rb gas was reported by Dudin and Kuzmich (2013) [23].

3. Experimental Setup

3.1. Optical setup

Our optical setup is reported in Appendix I. The lasers are in their respective housings and are frequency-locked to their respective atomic references. The specifics of laser locking is described in section 3.2. The cooling laser produces ~30 mW of power at the beam exit window at a diode current of 76.5 mA. An optical isolator (OI) is inserted into the cooling beam near its exit to extinguish feedback. The cooling beam is expanded to circular beam of diameter $\omega_{1/e^2} = 0.82 \pm 0.01$ cm by a $\times 5$ telescope to create a reasonably sized molasses region. After the expansion the cooling beam contains 10.2 ± 0.1 mW of power, corresponding to an intensity of $18.4 \pm 0.4\ \mathrm{mW/cm^2}$. The cooling beam is then split into three pairs of counter-propagating beams of intensities matched to within 10%. The three pairs form an intersection at the center of a glass cell into which one can dispense Rb vapor through a commercial getter. The quarter wave plates (QWPs) set the circular polarizations for each branch of the cooling beam to produce the trapping force. The repump beam contains ~10 mW of power and is expanded by a weak lens ($f \approx 25$ cm) to a 0.6 cm spot at the center of the intersection. The glass cell is raised above the laser beam exit level due both to the size of the ion pump and the convenience of creating the cooling beams perpendicular to the optical table. An anti-Helmholtz coil (details in 3.2) is placed over the glass cell to create a quadrupole magnetic field with $\vec{B} = 0$ at approximately the center of the molasses. The EOMs are driven by high voltage switching signals (details in 3.2) and modulate the intensities of the cooling and the repump beams. The probe beam contains ~10 mW of power at a driving current of 78.5 mA and is further attenuated down via a variable attenuator wheel. The probe beam is either a 1 mm × 1 mm circular spot or a 1.5 mm × 5.5 mm elliptical spot for the purpose of absorption spectroscopy or temperature and imaging measurements. The probe expansion is done by a × 5 anamorphic beam expander.

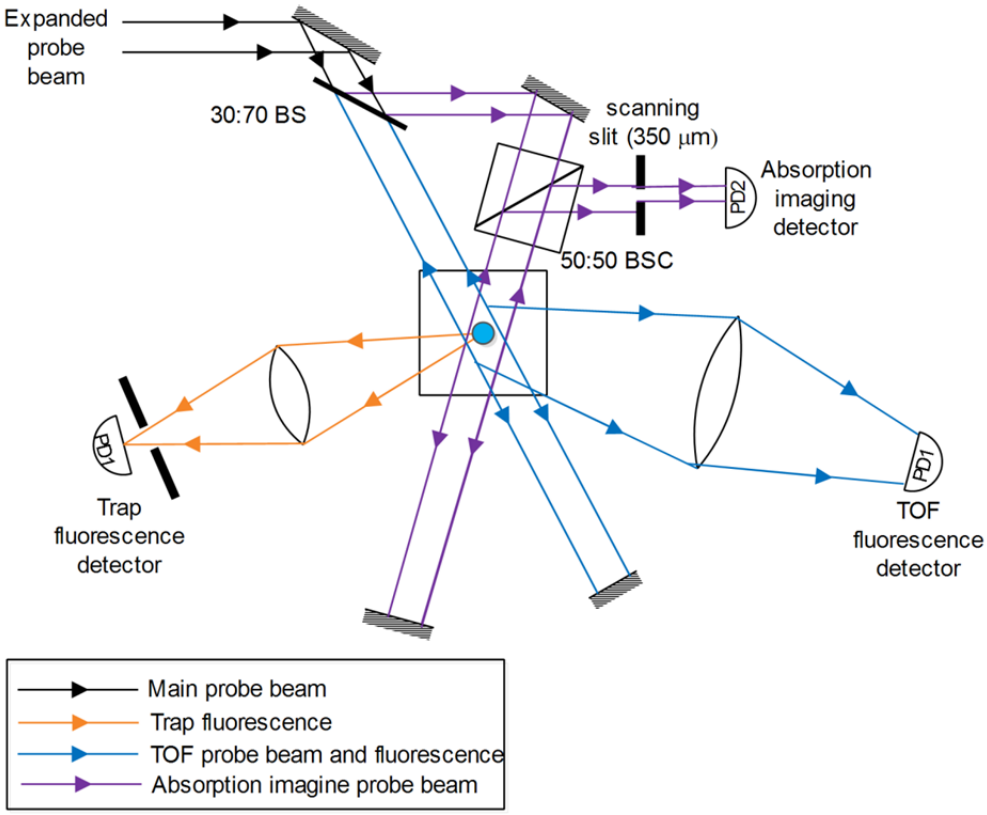

Figure 11 Near-trap optics

Figure 11 depicts the optics near the trapping region. The trapping and repump beams are omitted for clarity. These optics are set up to measure the trap population (orange beams), temperature (blue beams), and size (violet beams). The trap population is determined from the fluorescent light emitted by the trapped atoms as they cycle within the cooling transition (Eq. 3). The trap fluorescence is collected by $L1$ ($f = 7.5$ cm, $D = 6.0$ cm) and focused onto photodiode PD1 with an active region of $1\text{ cm} \times 1\text{ cm}$. The object distance s_o is set to 13.5 cm where the image distance s_i 40.5 cm. Thus the transverse magnification is ~3 times and thus a typical cloud of trapped atoms of 2 mm diameter will give a 6 mm image on PD1. The collection solid angle is $\Delta\Omega = \pi(D/2)^2/{s_o}^2 = 0.155\text{ sr}$. The probe beam is split into two portions with an intensity ratio of (blue : violet) ~7:3. The blue (violet) rays symbolize the probe beam used for TOF (absorption imaging) measurements. The TOF probe is back-reflected to form a 1-D

molasses and is placed at either 3 mm or 5.5 mm below the trapped atoms. A ~1 cm segment of the probe is imaged by $L2$ ($f = 6.5$ cm, $D = 5.5$ cm) onto PD2. The imaging probe is sent through a 50:50 non-polarizing beam splitter cube (BSC), through the trapped atoms, and then back-reflected to form a 1-D molasses. The return beam, now carrying absorption information, is reflected off of the BCS and coupled into PD2 through a slit of width 350 μm for intensity profile mapping. The slit is mounted on a micrometer driven translation stage.

3.2. Laser tuning/locking optics and electronics

Each of three ECDLs in our study is locked to a saturated absorption spectroscopy reference (SAS) signal. The optical setup required to produce a SAS signal as well as a block diagram illustrating the electronic components required for locking are given in Figure 12a. The arrows symbolize beams whereas electrical signal lines. 10% of the beam exiting the laser is picked off by a beam sampler to function as the SAS beam. The beam is reflected off of a glass slide to produce the signal and the reference beams (each containing ~4% of the total intensity)

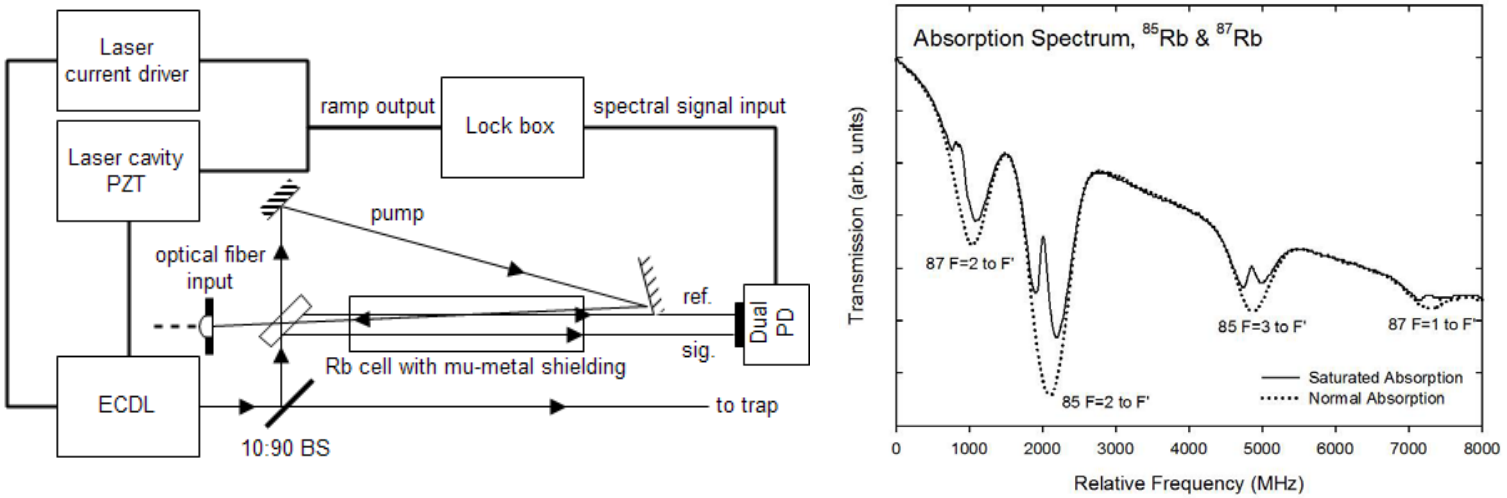

Figure 12 a) Saturated absorption spectrometer setup and locking block diagram; b) normal and saturated absorption spectra of Rb

which then propagate through a Rb vapor cell (pressure $\sim 10^{-7}$ torr). The transmitted portion is sent to propagate against the signal beam to function as an intense pump beam that saturates the absorption of the signal beam. The signal and reference beams are collected by photodiodes. The photocurrents generated are transconductance amplified into voltage signals and sent into both a viewing oscilloscope and the lock box. As the laser frequency ramps (driven by PZT and laser current driver), the probe and signal beams experience varying absorption as they transmit through the vapor cell, producing absorption spectra on the scope. In the reference spectrum (dotted line) one observes four Doppler-broadened absorption dips, each associated with a particular ground state to excited state transition, as discussed in Figure 1. The saturation effect of the pump beam is observed in the saturated absorption (signal) spectrum (solid line) from Figure 12b: the hyperfine transitions within each Doppler-broadened peak are saturated by the pump beam, resulting in increased transmission of the signal beam as its frequency scans over these resonances. The reference and signal spectra are then sent into the lock box for further processing. Details of the lock circuit are described in Appendix II. When locked the laser line width of the order 1 MHz, as determined by measuring the width of a hyperfine peak corresponding to a closed transition (e.g., ^{87}Rb $F = 2 \rightarrow F' = 3$ transition, see Figure 1). The measured width of the peak is ~7 MHz. The sloped background in Figure 12b is due to the change in laser intensity as its frequency is scanned.

3.3. Electro-optical modulators (EOMs), anti-Helmholtz trapping coil, and switching electronics

TOF, R&R (section 2.3), and as we shall see later, trap optical depth measurements all require the switching of both the beams and the trapping magnetic field. The typical time scales of these measurements are on the order of tens of milliseconds (Figure 5), which demands the beams and coils to be switched on a time scale of much less than a millisecond. Fast switching of laser fields are accomplished by EOMs driven by high voltage switching signals. The trapping field can be turned on and off by switching the current sent through the anti-Helmholtz coil.

An EOM contains birefringent crystals that rotate the plane of polarization of the input light field when a voltage is applied. The voltage that corresponds to 0° (90°) rotation in the polarization is termed V_0 ($V_{1/2}$) (a 90° rotation is equivalent to a half-wave retardation for a given wavelength). Now consider an EOM placed between a pair of polarizers with optical axes aligned in parallel. As the voltage applied to the EOM crystals is switched from V_0 to $V_{1/2}$, the input field switches from maximum to minimum transmission. The extinction ratio of the EOM is defined as the ratio between the transmitted intensity at V_0 to that at $V_{1/2}$. The response time of the EOM is typically limited only by the speed of the voltage switching electronics. For an AD*P crystal-based EOM, as used in our setup, the difference between V_0 and $V_{1/2}$ is typically within several hundred volts, and microsecond-switching can be readily achieved with JFET switches.

The zero-wave voltage (V_0), half-wave voltage ($V_{1/2}$) and the extinction ratio (R) of the two EOMs used in our optical setup are measured. The results for the cooling laser EOM are $V_0 = 120$ V, $V_{1/2} = -80$ V, and $R = 120:1$. The results for the repump laser EOM are $V_0 = 0$ V, $V_{1/2} = -375$ V, and $R = 60:1$. The extinction ratios are limited by depolarization due to unwanted reflections and/or stray birefringence. No cooling effect is observed when either or both EOMs are set to $V_{1/2}$, indicating the effectiveness of these specs.

The switching of the laser beams is accomplished by switching the voltage applied to the EOMs between V_0 and $V_{1/2}$. The positive terminal of the EOM is held at V_0 whereas the negative terminal is coupled to $V_{1/2}$ through a junction field effect transistor (JFET) and a pull up resistor ($\sim$1 MΩ). The JFET gate is driven by a 5 V TTL pulse with variable width from a signal generator. When the input at the gate of the JFET is low, the EOM operates at V_0 and the beam is on; when the input at the gate of the JFET is high, the resistor pulls the EOM to $V_{1/2}$ and the beam is off. Figure 13 shows the relevant signals for the cooling laser EOM. Figure 13a shows the TTL signal (yellow) and the corresponding voltage signal driving the EOM (blue). There exist a time lag of ~500 ns between the two traces; the EOM driving signal oscillates for ~1.5 µs before reaching steady level. Figure 13b shows the EOM driving signal (blue) and the corresponding light intensity signal (yellow) as measured by a battery-biased fast photodiode (Thorlabs DET210). One observes that the light signal faithfully follows the driving voltage signal. The beam intensity reaches baseline in ~1.5 µs, which is much faster than our TOF and R&R measurements demand. Similar behaviors are observed on the rising edge of the three signals.

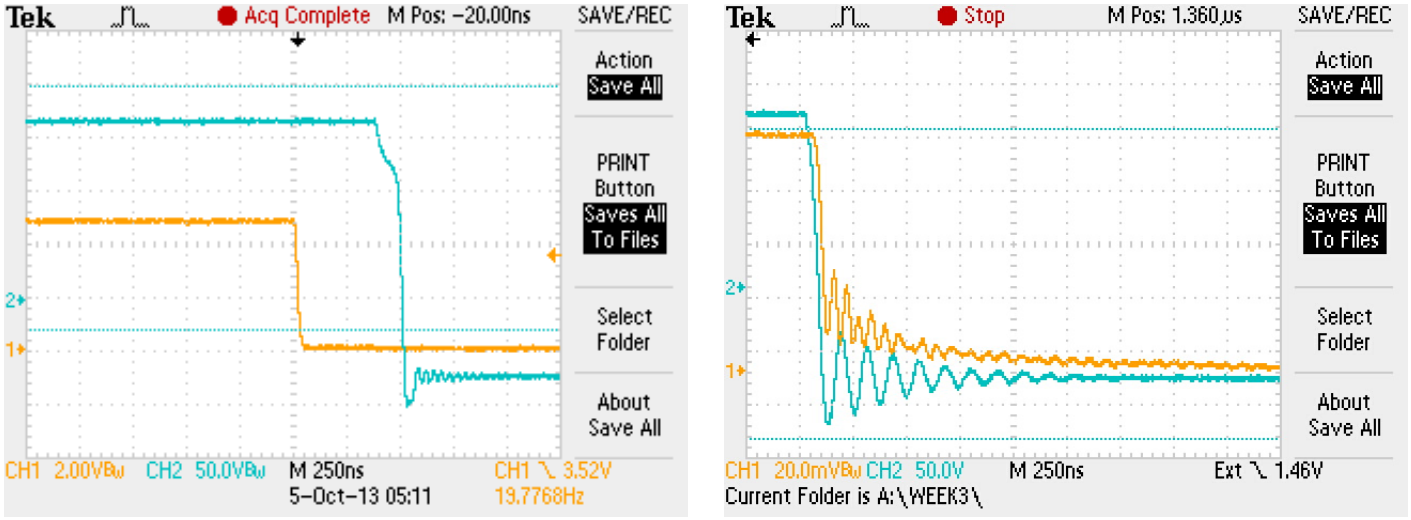

Figure 13 Time courses of signals

The anti-Helmholtz (Figure 14a) coil consists of two identical circular magnetic coils that are placed symmetrically along a common axis. The two coil rings, each of radius ~20 mm, are separated by a center-to-center distance of ~17 mm. The number of turns on each coil is ~200, matched to within 5% as determined by resistance measurements. The inductance of the coil is measured to be 1.9 mH and the resistance is 12.9 Ω.

The switching circuit for the coil is shown in Figure 14. The power supply is coupled through a high power rating bipolar junction transistor (BJT) to the magnetic coil. The BJT in series with the coil is triggered by a secondary BJT, which is in turn driven by a 5V TTL pulse. As the coil is switched off, the energy stored in the magnetic field discharges in the form of current through the 56 Ω power resistor and the 12.9 Ω coil self-resistance. The diode is inserted to prevent the current from flowing through the 56 Ω resistor when the coil is on. As the coil is switched off, the 1/e fall time of the current through the coil is measured to be 28 μs, which corresponds to the L/R time constant of the discharge loop 27.5 μs $[1.9\ \text{mH}/(56\ \Omega + 12.9\ \Omega)]$.

The response time of the trapping field to the coil current is limited by the following process. As the magnetic field is switched off, eddy currents are generated in nearby conducting objects. Eddy currents have a relatively long lifetime in good conductors (e.g., Al, Cu, etc.) Thus

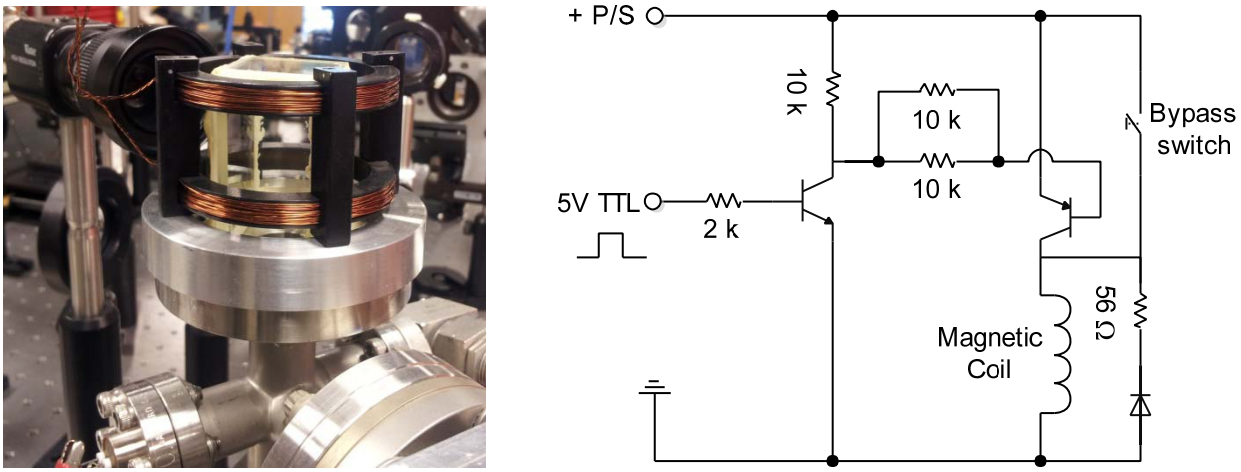

Figure 14 a) Anti-Helmholtz Coil ; b) Coil switching circuit

the eddy-induced secondary fields die off much more slowly compared to the primary field. Our first coil is formed on an aluminum body. The ring structures are favorable to eddy current flow. The fall time of the secondary field near the coil is measured by inductive pickup to be 500 μs, which is longer than desired. To minimize eddy currents we formed a second coil with identical specs out of a plastic (Ertalyte) body. The secondary field of the plastic coil falls in 28 μs, which accurately tracks the current falloff.

The same TTL pulse drives the EOM switches and the coil switch such that the beams and the field are switched in a synchronized manner.

3.4. Glass cell, vacuum assembly, and Rb getter

The glass cell for trapping is formed by pasting glass window pieces together with Torr Seal to form a five-sided rectangular block. The sixth side of the cell is sealed to a Conflat (CF) UHV flange with a 25 mm inner diameter on a five-way cross. The rest of the ports on the cross are connected to an ion pump, a roughing pump, a Rb getter, and a window flange. The entire assembly is roughed by a roughing pump and baked out prior to operation. The connection to the roughing pump is then sealed off with an UHV-compatible needle valve and the pump is detached from the system. The base pressure of the system is pumped to $\sim 10^{-8}$ torr through an ion pump. The pressure of the system is measured through the current the pump draws.

We use a commercial Rb getter to dispense Rb vapor into the glass cell for cooling and trapping. The getter is a Rb compound sitting inside a heating boat. Rb vapor is released as a current passes through the heater around the boat and heats up the compound, inducing a redox reaction. The onset for the reaction occurs at ~3.5 A of current and the Rb pressure increases exponentially as the current is turned up. The trap fill time at different heater currents are

measured. A steady current is passed through the heater and equilibrium between the dispensing and pumping rates are arrived. The fluorescence from the trapped atoms are collected and measured on PD1 (section 3.1). As the trapping beams are switched on the trap is gradually filled up to its steady state population. The optimum operating current is determined in section 4.2.

4. Preliminary Measurements

4.1. Vapor cell absorption

The model we developed in Appendix III for the transmission of a weak probe beam through a room temperature vapor cell under EIT condition must be consistent with the experimentally measured absorption in the absence of the control beam. Measurements are made on the room temperature transmission of a probe beam resonant with the two D_2 transitions in each isotope, respectively (Figure 1). To quantify the effect of saturation and find the weak probe limit, we measured the absorption as a function of the probe beam intensity. The results are presented in Figure 15.

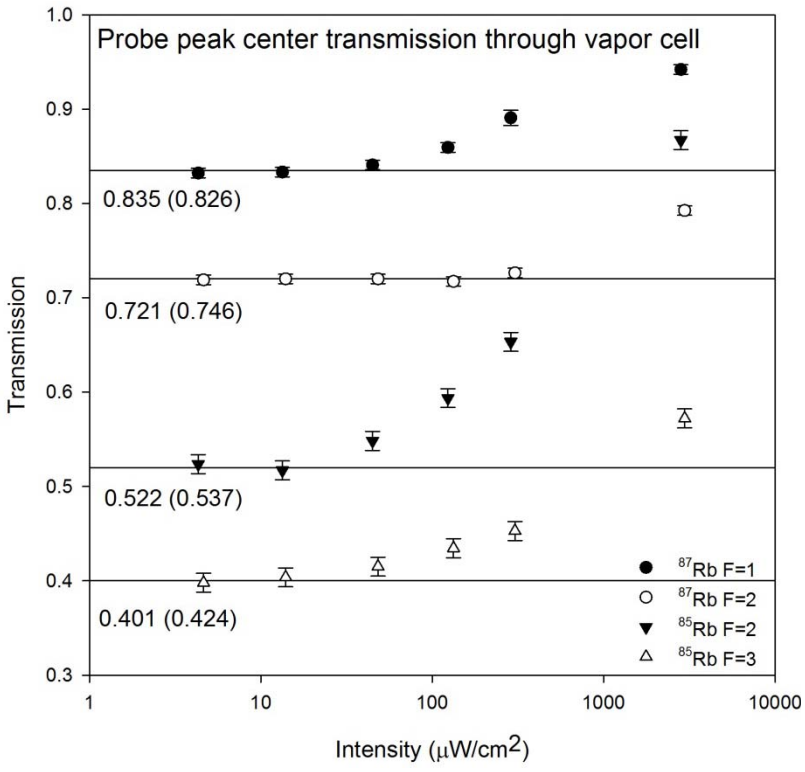

Figure 15 Probe peak center transmission through vapor cell

The peak center absorption for each transition is plotted as a function of the probe intensity. The measurements are made at $\sim T = 23.0$ ℃. Each curve tends to a limiting value as the probe intensity becomes smaller and smaller. This is consistent with the prediction by Equation 8 (section 5.2). We take the average of the last two data points on each curve to be the value for the unsaturated absorption. The values are indicated below the corresponding horizontal lines. The measured absorption values allow us to test the validity of the model for absorption developed in Appendix III (Equation AIII 7) in the limit of zero coupling intensity, i.e. $\Omega_C = 0$. The predicted peak center absorption values are given in the parentheses next to the measured values. We notice that all values agree to better than 6%. We attribute the differences to temperature fluctuations between measurements, which were on the 5% level. Thus the model in Appendix III is upheld in the limit where the coupling beam is absent. Our subsequent measurements on the probe absorption under EIT conditions were made in the weak probe limit, where probe intensity $< 10\ \mu W/cm^2$.

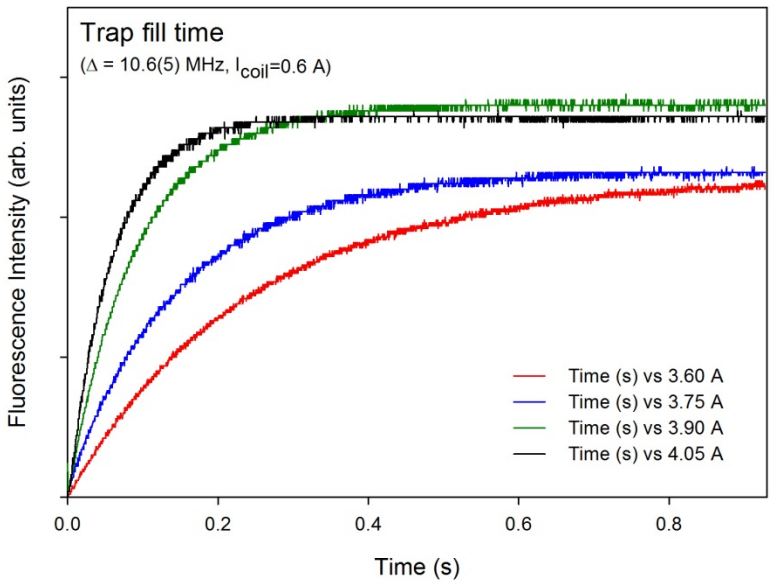

Figure 16 Trap fill time measurements at different heater currents

4.2. Trap fill time

The vapor density of Rb in the glass cell increases as the temperature of the getter heater is increased. The heater temperature is in turn proportional to the current. Under higher vapor pressure the MOT will load faster.

This is desirable for our TOF measurements in which the trap is emptied and then refilled many times to obtain an averaged signal, since a faster loading rate would enable us to repeat the process at a higher rate and enough signal samples can be acquired before the trap condition changes appreciably. A higher vapor pressure should also result in a higher steady state trap population, up till the pressure becomes so high that collisional loss limits the steady state population. In order to determine the optimum heater current that maximizes the steady state population but also gives a fill time $\ll 1$ s (the lowest rep rate we can set with the available instrument is 1 Hz), we measured, at different heater currents, the time course of the fluorescence from turning on the trap until the population (or fluorescent intensity) reaches steady state. The results are plotted in Figure 16.

The trap is turned on at $t = 0$. The trap population, which is proportional to the fluorescence intensity, grows approximately according to a $1 - e^{-t/\tau}$ behavior, where τ is the trap fill time. As the heater current is increased, from 3.60 A to 4.05 A, the trap fill time decreased from ~0.4 s to ~0.06 s. The steady state population is maximized for a current of ~3.90 A. At this current, the fill time is ~0.1 s, which satisfies the $\ll 1$ s requirement. Thus we operate the heater at 3.90 A for all subsequent experiments.

5. Experimental Results

5.1. Trapping a cloud of atoms

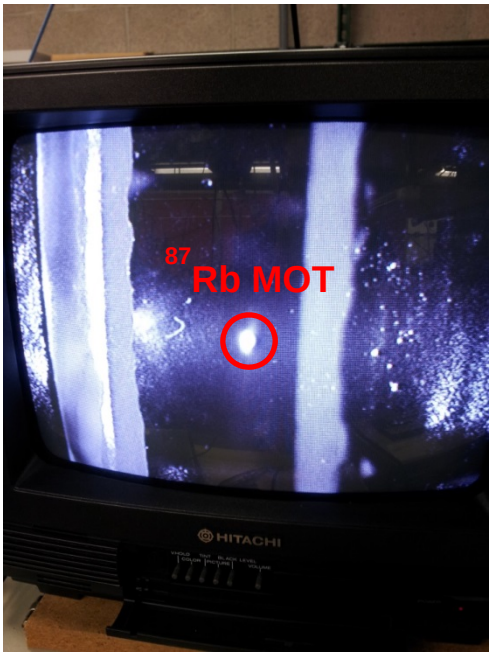

Figure 17 CCD image of trapped ^{87}Rb atoms

To trap a cloud of ^{87}Rb atoms we must prepare the lasers, the trapping field, and the Rb vapor. The cooling laser is tuned to the vicinity of $F = 2 \rightarrow F' = 3$ transition and locked at a frequency ~8-15 MHz red-detuned from the peak center. The repump laser is tuned and locked to the peak center of the $F = 1 \rightarrow F' = 2$ transition. Both EOMs are set to allow maximum transmission of the beams. The trapping field is turned on by delivering ~0.5-1.0 A of current to the coil. We then dispense Rb vapor into the glass cell by passing a 3.90 A current through the getter. As the Rb pressure in the cell increases the optical molasses region gradually lights up; a ball of Rb atoms starts to be visible at the center of the trap and steadily grows to its equilibrium size. A CCD image of the trapped atoms is shown in Figure 17. To estimate the trap population, we substitute the photocurrent of the fluorescent light from the trapped atoms collected by PD1 (Figure 11), the cooling laser intensity and detuning, and the detection solid angle into Equation 3. We estimate a trap population of $5.5(5) \times 10^8$ atoms. This is a reasonable amount of atoms for a MOT.

5.2. Trap absorption spectrum and population

The absorption spectrum for the of the cold atoms ($F = 1 \rightarrow F'$ transitions) is taken using the setup described in Figure 7 and compared to the saturated absorption (difference) spectrum obtained from a Rb vapor cell in Figure 12a. Each transition is labeled by its F' quantum number

(e.g., ν_2 correspond to $F = 1 \rightarrow F' = 2$). Each crossover resonance is labeled by the two F' quantum numbers that correspond to the two energy levels between which the resonance occurs (e.g., ν_{23} correspond to the crossover between $F' = 2$ and $F' = 3$). The bottom axis of the graph indicates the baseline for both spectra.

Note that the crossover resonances on the saturated absorption spectrum, which results from velocity selection effect of the counter propagating beams, are present in the saturated absorption spectrum but absent in the cold atom absorption spectrum. This indicates that the Doppler broadening effect has been significantly reduced by cooling (and therefore slowing down) the atoms. The linewidth of the ν_3 peak is measured to be 15 MHz, which is broader than the natural linewidth of the transition by 9 MHz. This is likely due to a combination of broadening effects including but not limited to residual Doppler-broadening, collisional broadening, power broadening, Zeeman shift broadening (due to the non-zero magnetic field in the trap away from trap center), and laser line broadening. How much each effect accounts for the 9 MHz excess broadening will be investigated further. Nevertheless, the linewidth provides an upper limit on the temperature of the trapped atoms. Suppose the 9 MHz broadening is due entirely to Doppler broadening, the corresponding temperature of the trap calculated using Equation 2 is ~100 mK. More definitive measurements (e.g, TOF, R&R) must be made to assess the actual trap temperature. These measurements will be discussed shortly. One also notices from Figure 12a that the actual transition strengths (as indicated by peak height) obtained from the cold spectrum differs from that indicated by the saturated absorption spectrum. The absolute absorption cannot be determined accurately from Figure 12a, as the absorption is strongly saturated by the cooling beams. The linear absorption coefficient of a sample as a function of the incident light intensity I is given by Equation 8

Equation 8

$$\alpha(I) = \frac{\alpha_0}{1 + I/I_s},$$

where α_0 is the linear absorption coefficient at $I = 0$ and is a Lorentzian function of the detuning $\omega - \omega_0$ in case of lifetime-broadened transitions ; and $I_s = \frac{\hbar^2\Gamma^2}{d^2}$ is the saturation intensity, where Γ is the natural linewidth and d is the electric dipole moment. For the ^{87}Rb $F = 2 \rightarrow F' = 3$ transition (ν_3 in Figure 12a), $I_s = 3.577\ \mathrm{mW/cm^2}$ whereas the cooling beams contain a total intensity of $I = 47.1\ \mathrm{mW/cm^2}$, making $\alpha(I) = 0.071 \times \alpha_0$. Similarly, the ν_1 and $\nu_2$transitions also suffer from saturation. In order to make a measurement of the unsaturated absorption of the sample, the cooling and repump beams must be shut off. We did not pursue this measurement in the current work.

The transverse density profile of the trapped atoms is determined by measuring the transverse intensity profile of the probe laser beam (frequency locked to the $F = 2 \rightarrow F' = 3$ transition) after it passes through the atom cloud. The 350 μm slit, mounted on a micrometer-

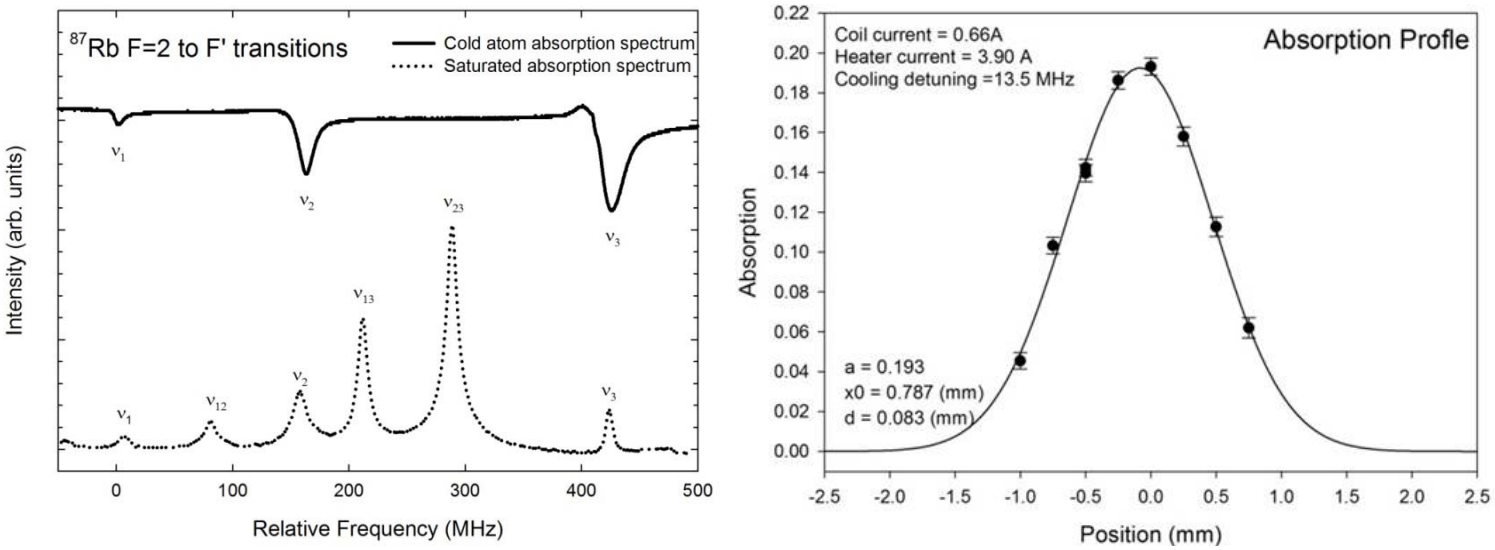

Figure 18 a) Absorption spectrum of cold atoms as compared to saturated absorption spectrum of warm atoms; b) transverse intensity profile of the probe after passing through cold atoms

controlled translational stage, is scanned across the probe laser beam in the transverse direction in 0.5 mm increments. The probe beam intensities in the presence and absence of the atomic cloud are recorded by PD 2 (Figure 11). The (single pass) absorption of the probe beam is calculated and plotted as a function of the slit position in Figure 18b. The profile of the cloud is fitted to a Gaussian function of the form

$$A = a\ \mathrm{Exp}\left[\left(\frac{x-d}{x_0}\right)^2\right],$$

where x is the position of the slit (x-axis on Figure 18b), a the peak absorption of the cloud, d the deviation of the center of the cloud from the arbitrarily defined zero point, and x_0 the $1/e^2$ radius of the cloud. The values of the fit parameters are given in Figure 18b. The trap conditions under which the measurement is made are also given in Figure 18b. The conditions include the magnetic coil current (which determines the magnetic field gradient and therefore the trap depth), the (getter) heater current (which determines the Rb deposition rate), and the detuning of the cooling laser (which determines the trap temperature and population). The ~1.6 mm cloud size is in agreement with the cloud size estimated from the CCD image. Note again that the absorption values in Figure 18b are the saturated values. Note also that our simple model assumes a uniform sample length along the direction of the probe, whereas the cloud is to a first approximation spherical. Thus our result is likely an underestimate of the cloud size.

We could understand the Gaussian distribution of the position of the atoms through the following simple argument. In any given spatial direction, the MOT provides a linear restoring force $F = -kx$ on each atom. Thus the potential along that direction is a harmonic potential, of the form $V(x) = 1/2kx^2$. Thus each atom (with maximum velocity v_{max} in the given direction)

undergoes simple harmonic motion $x(t) = A\sin(\omega t)$, where $A = \sqrt{m/k} \times v_{max} = v_{max}/\omega$ corresponds to the classical turning point of the motion. The root-mean-square (rms) position of the atom is given by

$$x_{rms} = \sqrt{\langle x^2 \rangle} = \left(A^2 \frac{\omega}{2\pi} \int_0^{2\pi} \sin^2(\omega t)\, dt \right)^{1/2} = \sqrt{\frac{1}{2}} A = \sqrt{\frac{1}{2}} \frac{v_{max}}{\omega}.$$

In other words, x_{rms} is proportional to v_{max}. Since particles obeying Maxwell-Boltzmann distribution has a Gaussian distribution of v_{max} along each spatial direction, x_{rms} is therefore also a Gaussian function. Physically this means that the faster moving atoms tend to stay near the edge of the cloud, whereas the slower moving ones tend to stay near the center. Since the width of the Gaussian function of v_{max} is related to the temperature of the MOT, one can deduce the temperature of the MOT from its size. However, due to the marginal spatial resolution of our measurement technique (350 μm slit vs. 2mm cloud) and the incompleteness of our model, the temperature determined this way is unreliable. In the following section we present a more deterministic way of measuring the trap temperature.

5.3.Trap temperature measurement using absorption time-of-flight

As we have mentioned in section 2.3, a TOF signal can be obtained by monitoring either the probe intensity or the fluorescence intensity as the atoms transit through. In practice, the collection of absorption signal, which is carried by the TOF probe beam, is much easier compared to that of the fluorescent light, which radiates in all directions. We were therefore able to obtain a much better signal-to-noise from absorption measurements, and thus it became our

preferred method for measuring the MOT temperature. Below we describe our measurement procedure and present the results.

Prior to the measurement, a cloud is prepared. A 0.5 mm diameter aperture is placed in the probe beam to define its center. The center of the probe beam is then scanned to line up with the center of the cloud by maximizing the absorption signal. The probe beam is then placed under the cloud, separated by distance d (Figure 19a), and frequency locked to the $F = 2 \rightarrow F' = 3$ transition. The probe beam is then back reflected onto itself (forming a 1D molasses) and imaged onto PD 2 (Figure 11), which is connected to an oscilloscope. At $t = 0$, all trapping beams and the magnetic coil are turned off, and the cloud is released. The off signal triggers the scope to start recording the signal from PD 2 as the atoms pass through the probe beam under free expansion and falling. This process is repeated several times for each measurement to improve the signal-to-noise. The repetition rate is set to 1Hz to allow the cloud to grow to its equilibrium size after each release. The center-to-center separation between the probe and the cloud d is varied between measurements. Since the cloud expands spherically to a first approximation, the peak absorption signal, which is inversely proportional to the density of the cloud, varies roughly as the inverse square of the separation. Thus longer averaging is required for larger d. The results are plotted in Figure 19. Each trace corresponds to a different d. The conditions under which the measurements are made is given in the top-left corner.

As the atoms of different velocities traverse the probe beam over time, they absorb the light, giving rise to a time-varying absorption signal on the oscilloscope. Since the absorption is proportional to the number of atoms, and the position of each atom (ignoring gravity) is the product of its initial velocity and the time-of-flight, this signal is essentially a mapping of the velocity distribution of the trapped atoms. The width of the trace increases as d increases from

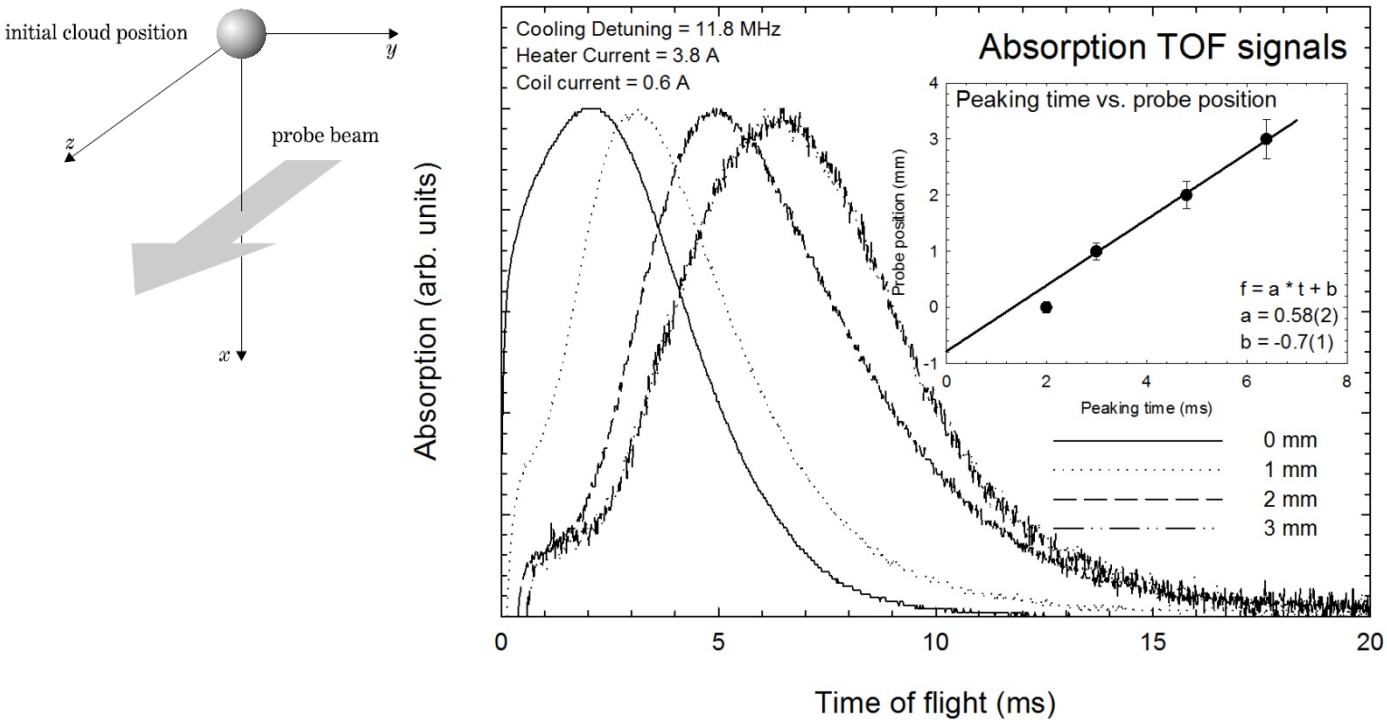

Figure 19 Absorption TOF measurements

1mm to 3mm. This is due to atoms of different velocities spread out in space as the time of flight increases. This translates into a spread in their arrival times. The time at which the absorption peaks divided by the flight distance d gives the most probable velocity v_p of the trapped atoms. If we assume a Maxwell velocity distribution, then $v_p = \sqrt{(2kT/m)}$. Thus by measuring v_p we can calculate the temperature of the cloud. The flight distance is plotted against the peaking time in the inset of Figure 19. The data points fall onto a straight line to a very good approximation, indicating that the mean initial velocity of the atoms in the cloud are too high for gravity to have an appreciable effect on the atom's velocity on a time scale of tens of milliseconds. The first data point, corresponding to $d = 0$, deviates appreciably from the straight line due to the fact that the peaking time is too close to $t = 0$, and the background subtraction results in large uncertainties in the absorption value within the first 100 μs after the shutoff (the imperfect background subtraction also results in the initial downward curving of the other traces). As a result, the first

data point is excluded from the fit. The result of the weighted linear fit indicates a slope of $v_p = 0.58 \pm 0.02$ m/s. This corresponds to a temperature of 1.8 ± 0.1 mK. Within the first 10 ms, gravity accelerates the atoms by no more than 0.1 m/s. This is a 15% or below correction to each data point in the fit, which is within the error bar of each point from estimating the peak position. The actual error bar on the temperature is expected to be somewhat larger due to the oversimplification of our model. Note that our fit predicts a negative. This temperature is consistent with a typical temperature obtained in a MOT, namely on the order of 100 μK to 1 mK. We were unable to record TOF traces for d larger than 3 mm due to poor signal-to-noise.

Using the TOF technique we proceeded to studying the dependence of trap temperature on the detuning of the cooling laser. We placed the probe beam at $d = 3$ mm away from the cold atoms and recorded the TOF peaking time as the cooling detuning is varied from 8 to 25 MHz. The trap temperature corresponding to each TOF peaking time is calculated using the method described in the previous paragraph. The trap temperature as a function of detuning is plotted in Figure 20a. The number of trapped atoms is also measured for each detuning value using the

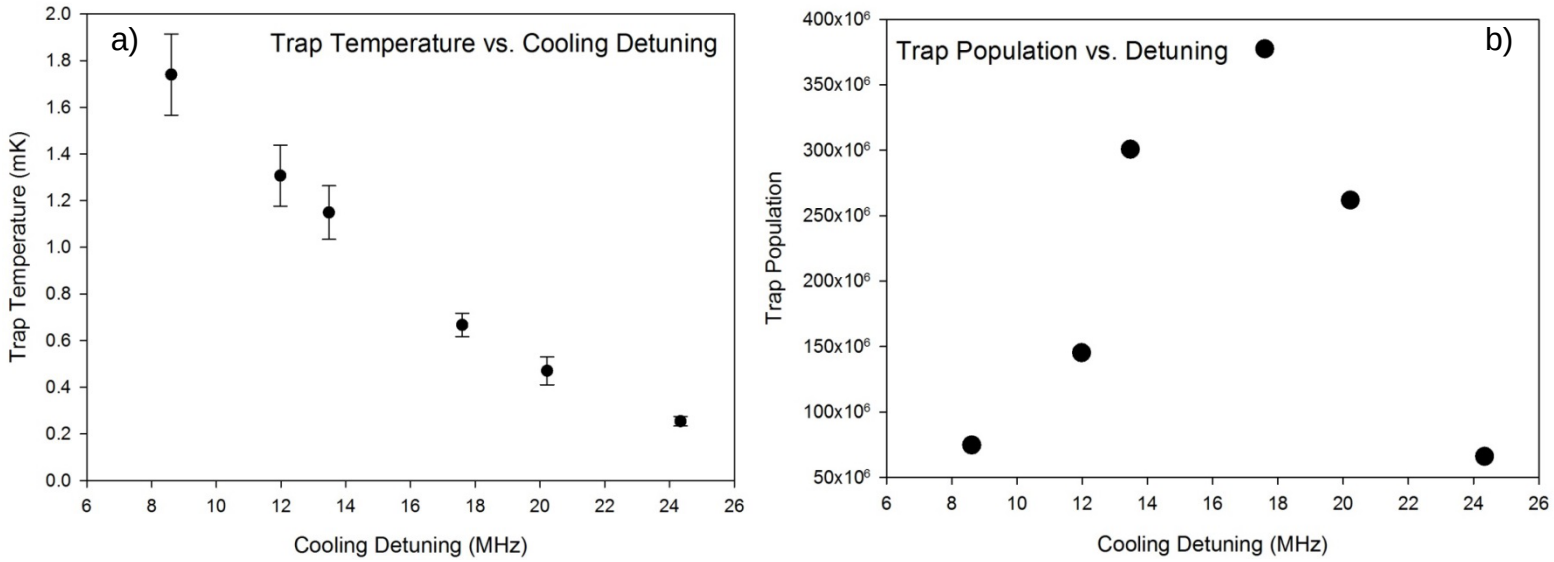

Figure 20 a) Measured trap temperature as a function of cooling laser detuning; b) measured trap population as a function of cooling laser detuning

fluorescence intensity measured by PD2 and plotted in Figure 20b. Because increased red detuning means the laser will be on resonance with atoms of higher velocity class traveling against the laser beams, we expect the trap temperature to decrease with increased red detuning. This prediction matches with our observation. The number of trapped atoms peaks at around 18 MHz and decreases to below noise level on PD2 as we increase the detuning to above 25 MHz. At 24.4 MHz, the measured trap temperature is ~200 μK. This is approaching the Doppler cooling limit given by

$$T_D = \frac{\hbar\Gamma}{2k_B},$$

where Γ is the resonance scattering rate of the cooling transition. This limit corresponds to the fact that the cooled atoms in the trap can still scatter photons from the cooling beam, leading to residual motion and therefore heating. For the ^{87}Rb cooling transition $T_D \approx 150$ μK. Due to the diminishing trap population, more sensitive fluorescent detection is required to explore the trap temperature variation near the Doppler cooling limit.

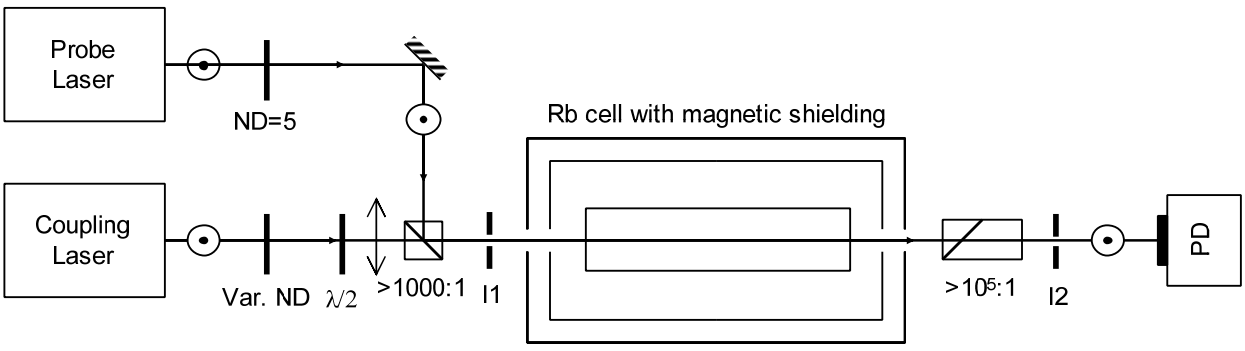

Figure 21 Experimental setup for studying EIT in a warm vapor cell with a coaxial probe-coupling geometry.

5.4. EIT in a warm vapor cell

Our experimental setup for studying EIT in a warm vapor cell is shown in Figure 21. The probe and coupling beams are produced from two respective ECDLs. The are linearly polarized in orthogonal directions and combined at a polarizing beam splitter (PBS) with extinction ratio better than 1000:1. The two beams co-propagate through a path defined by two irises (I1 and I2) with crossing angle < 5 mrad. A magnetically shielded Rb vapor cell (7.5 cm long) is placed midway between I1 and I2. The probe laser is attenuated by an ND filter with $\mathrm{OD} = 5$ to an intensity of $\sim 5\ \mu\mathrm{W/cm^2}$, within the non-saturating intensity regime ($< 10\ \mu\mathrm{W/cm^2}$) as determined from section 4.1. The waist of the coupling beam ($647\ \mu\mathrm{m} \times 1133\ \mu\mathrm{m}$) is placed at the center of the cell. The coupling beam area varies by no more than 10% over the length of the cell. Since the probe beam has a much larger area than the coupling beam, I2 is set to expose the center ($356\ \mu\mathrm{m} \times 478\ \mu\mathrm{m}$) portion of the probe beam to the photodiode (PD). The coupling beam is then separated away from the probe beam path through a double Glan-Taylor prism, with extinction ratio better than 10^5:1. The probe intensity is recorded by the PD, which is transconductively amplified and fed to an oscilloscope synched with the ramp driving the probe

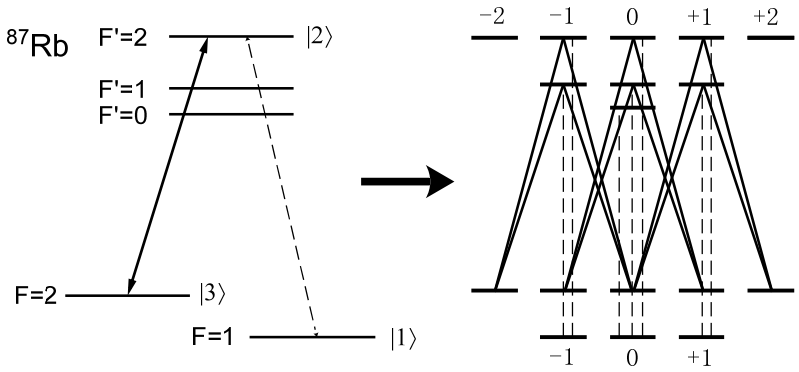

Figure 22 overall (left) and detailed (right) probe and coupling transitions

laser.

We chose to study the Λ-type EIT system in ^{87}Rb shown in the inset of Figure 23b. To our best knowledge this scheme has not been studied previously in a vapor cell or in cold atoms. The probe beam (dashed line) probes from $F = 1$ to all F' levels and the coupling beam is frequency locked to the $F' = 2 \leftrightarrow F = 2$ transition. The two-photon EIT condition is satisfied when the probe and coupling frequencies differ by exactly the frequency difference between $F = 1$ and $F = 2$, which is 6.8 GHz. Since the Doppler profiles of the $F = 1 \rightarrow F = 0,1,\text{and } 2$ transitions overlap significantly (at room temperature, $\Delta\nu_D \approx 530$ MHz, $\nu_{1\rightarrow 0} - \nu_{1\rightarrow 2} = 229$ MHz), the two-photon condition is simultaneously satisfied for the $F' = 2$ and the $F' = 1$ states (the $F' = 0$ state is not dipole coupled to the $F = 2$ state). The complete set of probe and coupling transitions for orthogonally polarized beams are shown in Figure 22. The π polarized probe beam connects levels of equal m_F number. The coupling beam is decomposed into σ^+ and σ^- components for the purpose of analysis [27]. Each probe transition is connected by a coupling transition is connected by a coupling transition to the $F = 2$ ground state, except for the $F = 1, m_F = 0 \rightarrow F = 0, m_F = 0$ transition. In other words, this EIT system is incomplete. However, due to the relatively small matrix element of the $F = 1 \rightarrow F' = 0$ transition ($g_{10}{}^2 = 1/6$) comparing to those of the $F = 1 \rightarrow F' = 1$ and $F = 1 \rightarrow F' = 2$ transitions ($g_{11}{}^2 = 5/12$, $g_{12}{}^2 = 5/12$), we do not expect this defect to impact the atomic coherence significantly. Since the probe and coupling beams are co-propagating, atoms of the same velocity class will experience approximately the same Doppler shift in the frequency of both beams. This means the two-photon EIT condition is satisfied for atoms at any velocity, relaxing the requirement of having a strong coupling beam to establish the atomic coherence.

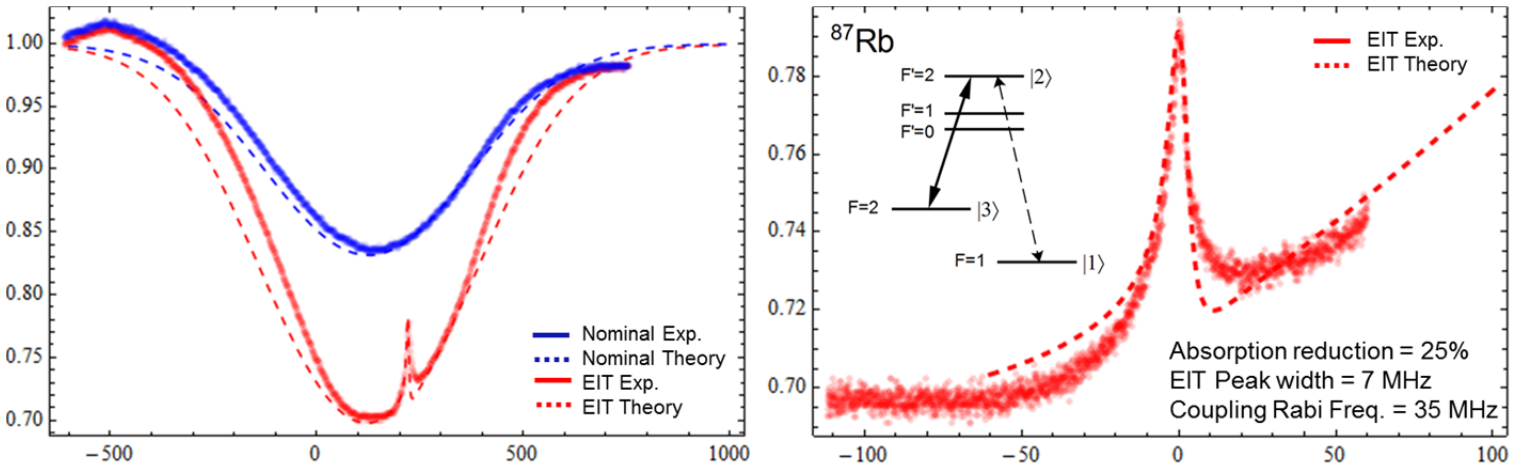

Figure 23 a. nominal (blue solid) and EIT (red solid) absorption spectra of the probe beam, with fits (blue dashed and red dashed) generated from the model in Appendix III. b. The EIT transparency peak; the fit is in good agreement with the data.

The absorption spectrum of the probe beam is measured both in the absence (blue) and the presence (red) of the coupling beam (Figure 23a). An EIT transparency peak is observed on the blue curve at 228.1 MHz (relative to the $F = 1 \rightarrow F' = 0$ resonance, which is defined to be 0 MHz), corresponding to the two-photon transition frequency. The peak has width of 7.0 ± 0.1 MHz FWHM and corresponds to a $25 \pm 1\%$ reduction in the probe absorption. The maximum absorption increased by a factor of 1.95, close to the predicted doubling of population density due to the optical pumping effect from the coupling beam. Fit curves are generated using the model developed in Appendix III (Equation AIII 7). Best fit near the EIT peak (Figure 23b) is found by setting $\gamma_{31} = 2\pi \times 3$ MHz, $\gamma_{23} = \gamma_{21} = 2\pi \times 6$ MHz ,and $\Omega_c = 2\pi \times 40$ MHz. Recall that in the presence of finite laser linewidth, γ_{31} is the sum of the decoherence rate between the $F = 1$ and $F = 2$ ground states and the linewidths of the probe and coupling lasers (i.e., $\gamma_{31} \rightarrow \gamma_{31} + \gamma_p + \gamma_c$). Our laser linewidths, estimated from the broadening of saturated absorption peaks, are $\gamma_p = \gamma_c = 2\pi \times 1.5$ MHz. The value for γ_{31} is taken to be $2\pi \times 0.1$ MHz from ref. 25, which studies a EIT system involving the $D1$ transitions in room temperature Rb vapor cell. Therefore $\gamma_{31} = 2\pi \times 3.1$ corresponds to our experimental conditions. This value is

in good agreement with that determined form the fit. An estimate for the coupling Rabi based our coupling intensity $I_c = 3.67\ \mathrm{W/cm^2}$ can be obtained from the following relation

$$\Omega_c = \frac{g_{eff}^2 \times \mu_{F=2\to F'=2}}{\hbar} \times \sqrt{\frac{2I_c}{\epsilon_0 c}} = g_{eff}^2 \times 2\pi \times 232\ \mathrm{MHz}\,.$$

However, an estimate the effective coupling strength g_{eff} is made difficult by the complex quantum dynamics of the simultaneous EIT systems between different Zeeman sublevels. The Rabi frequency $\Omega_c = 2\pi \times 40$ MHz from the fit to the experimental data is not inconsistent this estimate. The global fits (Figure 23a) show 10% larger Doppler widths comparing to our measurements in the cases of nominal and EIT absorption. This is due to the fact that we calibrated our data using the saturated absorption peaks on the probe laser reference spectrum, which is distorted due to optical pumping effects. Overall, the model is in good agreement with the data. The model predicts the transparency to increase linearly with the coupling laser Rabi frequency when it is not too high ($\Omega_c < 200$ MHz). This can be potentially achieved by focusing the coupling laser down using a lens to obtain higher coupling intensity. This is not, however, pursued in the current work. We also expect improved transparency in cold atoms, since the Doppler profiles of the transitions are now isolated and the EIT system in Figure 23b no longer suffers from incompleteness as in the case of warm atoms. To accurately measure an EIT spectrum in cold atoms one must switch off the MOT and probe the atoms before they become too dilute. This requires fast (< 1 ms) switching of four laser beams. Progress is being made towards this direction.

6. Conclusion

We have constructed and characterized a magneto-optical (MOT) trap of ^{87}Rb atoms for the purpose of studying EIT as well as EIT-based light storage in cold atoms. The absorption spectrum of the atoms in the MOT was measured. The MOT was characterized in terms of its number of atoms, size, and temperature. The number of atoms was estimated form the trap fluorescence to be $\sim 5 \times 10^8$. The size of the MOT was measured using spatially-resolved absorption spectroscopy to be ~ 1.6 mm. The temperature of the MOT was measured using the time-of-flight technique as a function of cooling laser detuning. The coldest trap temperature achieved was ~ 220 μK, approaching the Doppler cooling limit for Rb $T_D = 150$ μK. Electromagnetically-induced transparency was studied in a Λ-type scheme in warm ^{87}Rb atoms, where the coupling laser couples the $F = 2 \rightarrow F'$ transitions and the probe laser probes the $F = 1 \rightarrow F'$ transitions. We achieved 25% peak reduction in the probe absorption. Both normal and EIT absorption spectra are calculated from first principle. The experimental results were in good agreement with the calculations. This work forms the basis for studying EIT and eventually storing light in cold Rb atoms.

Appendix I: Optical Setup

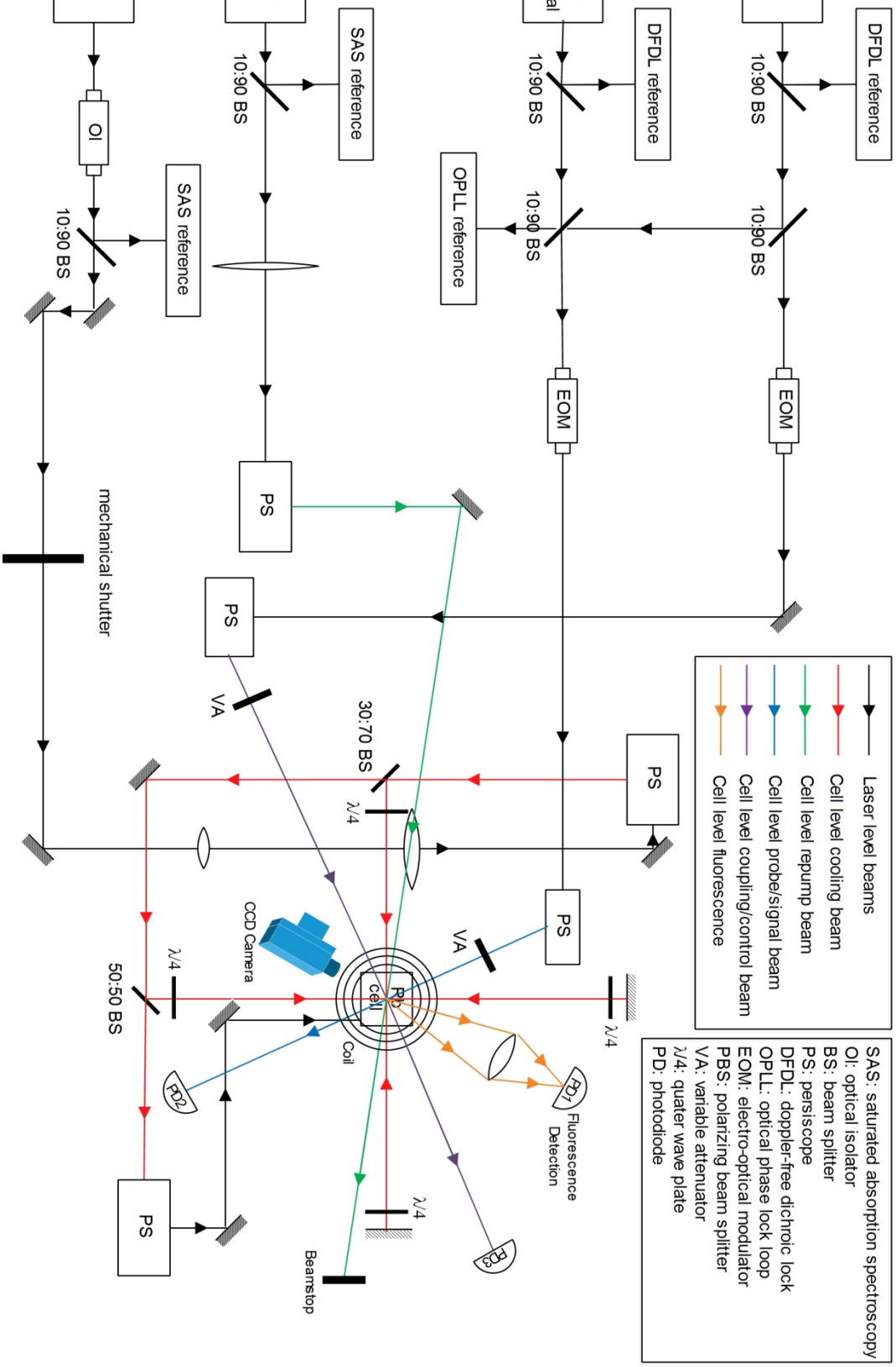

Figure A 1 Figure A 2 Proposed optical setup for laser cooling and trapping as well as EIT based slow light and light storage experiments. The lasers in their respective housings and are frequency-locked to their respective atomic references. The probe and coupling lasers are further phase-locked to each other. The Rb cell is vacuum pumped to ~10^{-7}-10^{-8} torr by an ion pump, which is omitted in the setup. The production of Rb in the cell is achieved by heating a commercial Rb getter. The Rb cell is raised above the laser beam exit level due both to the size of the ion pump and the convenience of creating the cooling beams perpendicular to the optical table. The cooling beam is expanded to a circular beam of diameter ~1 cm to create a reasonably-sized molasses region. The repump beam is expanded by a weak lens to flood the cell. The EOMs control the on/off of the probe and coupling beams. The variable attenuators control the intensities of the coupling and probe beams. All photodiodes are transconductively amplified.

Appendix II: Laser Lock Circuit

Figure AII1 in the previous page shows the schematic for the lock box and Figure AII2 shows the printed circuit board (PCB) designed according to the schematic. Our design is a modification based on the design by MacAdam *et al.* (1992) []. The lock box functions both as a PZT driver and a frequency feedback controller. We first describe the PZT driver part of the circuit. A triangular voltage ramp ($V_{pp} = 5$ V, Frequency $= 10$ Hz) driving the PZT is generated using the combination of an integrator ("Int", $\tau = RC = 0.1$ s) and a voltage comparator ("Comp"). The ramp is then coupled to the output op-amp ("Output") through the "Ramp Gain" trim pot that controls the size of the ramp. An adjustable DC bias is added to the ramp through the "Ramp Bias" trim pot. The drive signal from "Output" is amplified through a high voltage amplifier and sent to the laser module housing the PZT. The drive signal is also fed into the laser current driver (Figure 8a). The laser driver converts the drive voltage into a current signal, which acts as a small modulation of the laser current around the current set point. This allows for synchronized tuning of the PZT and the laser diode current to achieve a wideband (~9 GHz) mode-hop-free frequency tuning.

Next we describe the how the box provides locking and feedback to the laser. Using photodiodes we measure a saturated (normal) spectrum for the signal (reference) beam synchronized with the drive. The signal and reference spectra are buffered by "PD2" and "PD1", respectively, and then sent into the difference amplifier "Diff". The difference signal provides the hyperfine frequency spectrum we reference and lock to (see Figure 8b). An adjustable DC bias is added to the difference signal through the "Set Point" trim pot. The "Error" op-amp acts as a low-pass filter with cutoff frequency of 15.4 Hz. This filters out the high frequency noise as

they will cause the PZT to oscillate. The error signal at the output of “Error” is then coupled into “Output” through the loop gain trim pot. The laser frequency is locked through the following procedure. The laser is tuned to ramp over the target group of hyperfine peaks and the ramp bias and ramp gain are adjusted to move to and zoom in on the desired side of the target peak on the difference signal. The lock point on the error signal is then brought to cross $V = 0$ as observed on an osci1loscope. The loop gain is gradually increased so that the circuit can correct for deviations from the lock point and holds the frequency near the side of the peak. The lock point can be moved from approximately 10% to 90% of the peak value by adjusting the ramp bias or the set point. Once locked the noise (due to change in laser frequency) on the difference signal is fed back into the laser module via the following ways depending on its frequency components. The slow components (< 16 Hz, e.g. external temperature and pressure changes, etc.) are fed onto the slow PZT; the fast components (> 16 Hz, e.g. electronic noise, acoustic and mechanical vibrations, small uncontrolled optical feedback, etc.) are fed onto both the fast PZT and the laser diode. The fast feedback is either amplified by “FPZT Mod” and coupled to the fast PZT via a high-pass filter, or amplified by “I Mod” and coupled to the laser diode via a high-pass filter. On both “FPZT Mod” and “I Mod” we have an option to switch one of the inputs to an external modulation. In summary, a wideband feedback loop is formed between the laser, the spectrometer, the lock box, and the laser frequency driving components (PZT and current driver).

All op-amps on the board are low-noise, low input offset OP07 op-amps, with unity gain bandwidth 0.6 MHz. The power supply for the board is provided by a standard bipolar AC-to-DC converter. The schematic for the circuit is shown in the inset of the schematic diagram.

Servo Lock Box Circuit Diagram

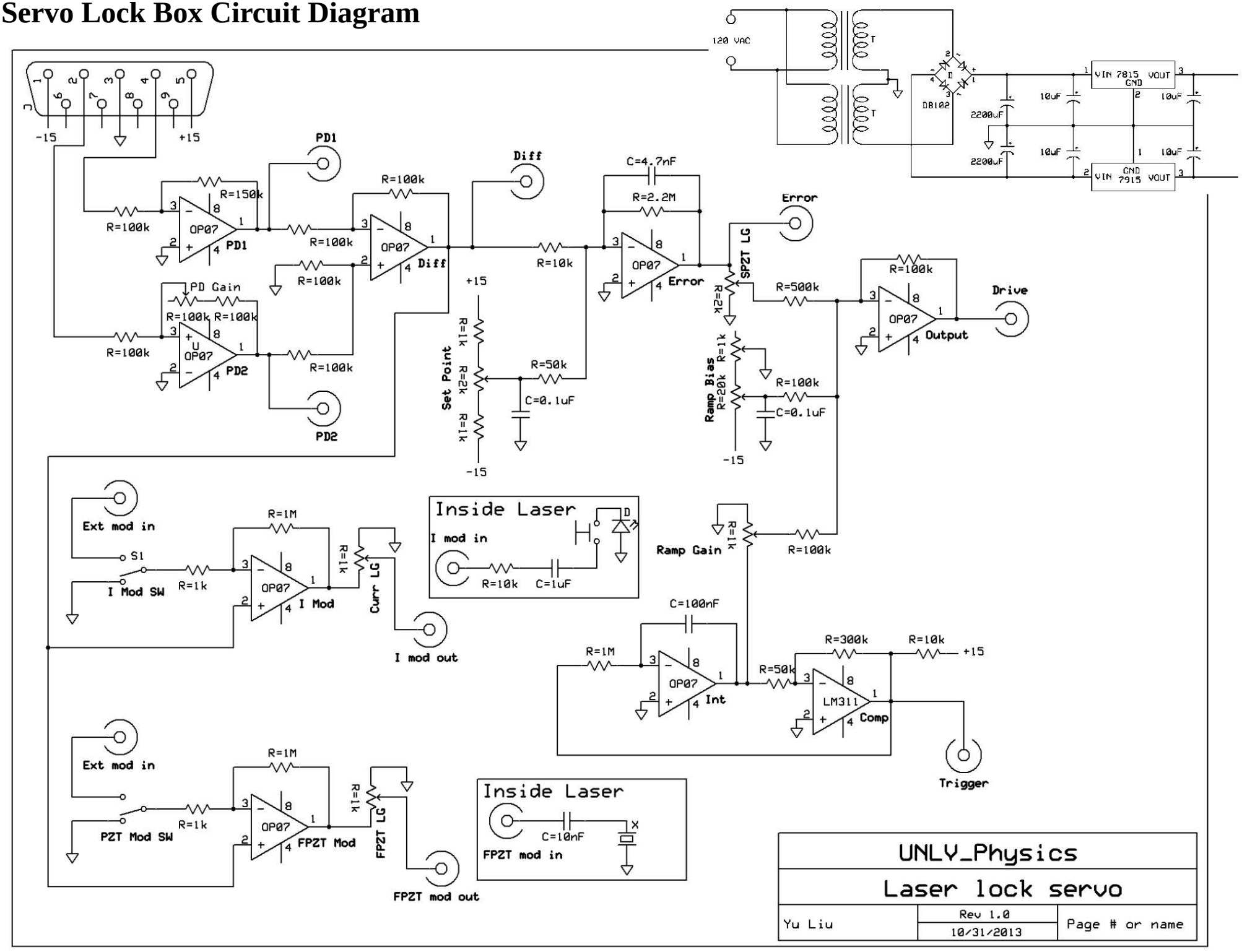

Figure AII 1 Laser lock and power supply schematics

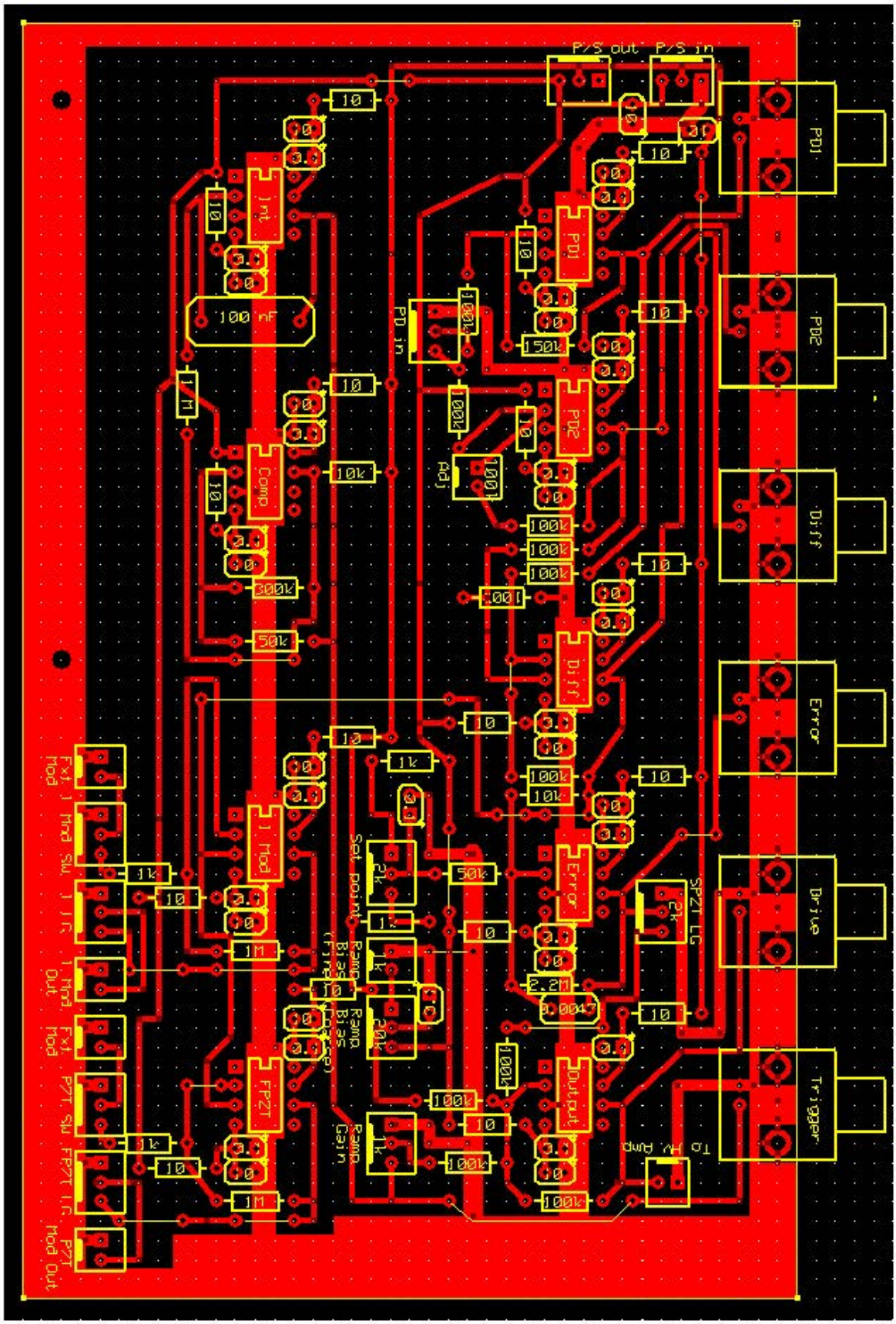

Figure AII 2 Laser lock printed circuit board layout

Appendix III Electromagnetically-Induced Transparency

A3.1. Solutions to the 3-level optical Bloch equation

Here we shall derive the semi-classical formalism that leads to EIT for an ensemble of closed Λ-type three-level atoms. We follow the development by Scully and Zubairy [27]. The energy levels of the atoms are described in Figure AIII 1, with states $|1\rangle$ and $|2\rangle$ coupled by a weak probe field of frequency ω_p and $|3\rangle$ and $|2\rangle$ by a strong coupling field of frequency ω_c. $|1\rangle$ and $|3\rangle$ are coupled by a Raman (forbidden) transition. We are interested in the dispersion and absorption of the probe field. The intensities of the probe and coupling beams are characterized by their respective complex Rabi frequencies

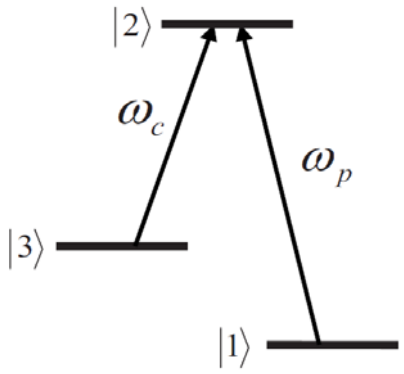

Figure AIII 1

$$\Omega_p e^{-i\omega_p t} \qquad \text{and} \qquad \Omega_c e^{-i\varphi_c} e^{-i\omega_c t}$$

And since the probe field is weak and the absorption and dispersion properties we are interested in are determined by the polarization to the lowest order in the electric field amplitude, ε, the probe Rabi frequency can be rewritten as

$$\frac{\mu_{21}\varepsilon}{\hbar} e^{-i\omega_p t},$$

where μ_{12} is the dipole matrix element given by $\mu_{21} = e\langle 2|r|1\rangle = \mu_{12}^*$. The coupling is strong and therefore must be treated exactly.

The Hamiltonian of an atom can be written as the sum of the ground state Hamiltonian H_0 and the light-atom interaction Hamiltonian H_I

$$H = H_0 + H_I,$$

where

$$H_0 = \hbar\omega_1|1\rangle\langle 1| + \hbar\omega_2|2\rangle\langle 2| + \hbar\omega_3|3\rangle\langle 3|$$

and

$$H_I = -\frac{\hbar}{2}\left(\frac{\mu_{21}\mathcal{E}}{\hbar}e^{-i\omega_p t}|2\rangle\langle 1| + \Omega_c e^{-i\varphi_c}e^{-i\omega_c t}|2\rangle\langle 3|\right).$$

The finite lifetime of the atomic states (due to spontaneous emission, collisions, etc.) are accounted for by the relaxation operator Γ whose matrix elements are given by $\langle i|\Gamma|j\rangle = \gamma_{ij}$.

Now, at any given time t the state of the atom can be regarded as some superposition of the three states and can be written in the form

$$\left|\psi(t)\right\rangle = c_1(t)e^{-i\omega_1 t}\left|1\right\rangle + c_2(t)e^{-i\omega_2 t}\left|2\right\rangle + c_3(t)e^{-i\omega_3 t}\left|3\right\rangle.$$

For a single atom, its state can be found by solving the Schrödinger equation $i\hbar\frac{\partial|\psi(t)\rangle}{\partial t} = H|\psi(t)\rangle$. For an ensemble of atoms as in this case, we use the density matrix approach. The density operator for the system under consideration is defined as $\rho = |\psi\rangle\langle\psi|$. To determine the state of the ensemble as time evolves we are interested in the time evolution of the matrix elements of ρ. The time development of ρ can be obtained by solving the Heisenberg equation of motion $\dot{\rho} = -\frac{i}{\hbar}[H,\rho] - \frac{1}{2}\{\Gamma,\rho\}$. The matrix elements of ρ therefore obey the relation

$$\langle i|\dot{\rho}|j\rangle = -\frac{i}{\hbar}\langle i|[\rho, H]|j\rangle - \frac{1}{2}\langle i|\{\Gamma, \rho\}|j\rangle$$

The equations of motion for the density matrix elements ρ_{12}, ρ_{23}, and ρ_{13} are therefore given by

$$\dot{\rho_{21}} = -(i\omega_{21} + \gamma_{21})\rho_{21} - \frac{i}{2}\frac{\mu_{21}\mathcal{E}}{\hbar}e^{-i\omega_p t}(\rho_{22} - \rho_{11}) + \frac{i}{2}\Omega_c e^{-i\varphi_c}e^{-i\omega_c t}\rho_{31}$$

$$\dot{\rho_{31}} = -(i\omega_{31} + \gamma_{31})\rho_{31} - \frac{i}{2}\frac{\mu_{21}\mathcal{E}}{\hbar}e^{-i\omega_p t}\rho_{32} + \frac{i}{2}\Omega_c e^{i\varphi_c}e^{i\omega_c t}\rho_{21}$$

$$\dot{\rho_{32}} = -(i\omega_{23} + \gamma_{23})\rho_{32} + \frac{i}{2}\frac{\mu_{21}\mathcal{E}}{\hbar}e^{-i\omega_p t}\rho_{31} - \frac{i}{2}\Omega_c e^{-i\varphi_c}e^{-i\omega_c t}(\rho_{22} - \rho_{33})$$

In a typical light storage experiment, the coupling field is on before the arrival of the probe pulse, and the atoms are optically pumped to state $\langle 1|$ at $t = 0$. Thus we have the initial condition

$$\rho_{11}^{t=0} = 1, \quad \rho_{22}^{t=0} = \rho_{33}^{t=0} = \rho_{32}^{t=0} = 0$$

With these initial conditions we obtain the following steady-state solution

Equation AIII 1

$$\rho_{21}(t) = \frac{i\mu_{21}\varepsilon e^{-i\omega_p t}}{2\hbar}\frac{1}{\gamma - i\Delta + \frac{{\Omega_c}^2}{\gamma_{31} - i(\Delta - \delta)}} = \frac{(i\Omega_p/2)\, e^{-i\omega_p t}}{\gamma - i\Delta + \frac{{\Omega_c}^2}{\gamma_{31} - i(\Delta - \delta)}},$$

where the coupling field detuning is $\delta = \omega_{23} - \omega_c$, the probe field detuning is $\Delta = \omega_{12} - \omega_p$, and $\gamma = (\gamma_{21} + \gamma_{31} + \gamma_{23})/2$.

A3.2. The real and complex susceptibility of the ensemble

The absorptive and dispersive properties of the ensemble are given by its complex susceptibility χ. χ is related to the complex polarization of the ensemble P through

$$P = \epsilon_0 \chi \varepsilon, \qquad \text{where} \qquad P = 2N\mu_{21}\rho_{21}e^{i\omega_p t}$$

Therefore we can express χ in terms of ρ_{12} as

Equation AIII 2

$$\chi(\Delta, \delta) = -\frac{2N{\mu_{21}}^2}{\hbar\Omega_p}\rho_{21} = 2Ng^2\rho_{21},$$

where we have made the substitution $g^2 = \frac{|\mu_{12}|^2}{\hbar\epsilon_0}$. g is termed the atom-field coupling constant since it is proportional to the dipole moment of a transition and therefore characterizes the strength of the coupling. For example, the effective dipole moment for the ^{87}Rb $F = 2 \rightarrow F' = 3$ transition is $\mu_{12} = 1.731 \times 10^{-29}$ C · m, making $g^2 = 3.207 \times 10^{-13}$ m^3.

Now, χ is given in terms of its real and imaginary parts as $\chi = \chi' + i\chi''$, where χ'' determines the absorptive property of the ensemble, and the transmission of the probe field is given by

$$T(\Delta, \delta) = e^{-\chi'' k_p L}, \qquad \text{or near resonance } (\Delta \approx \delta), \quad T(\Delta) \approx e^{-(\Delta/\Delta\nu)^2},$$

where as χ' determines the dispersive property of the ensemble, and the index of refraction of the medium to the probe is given by

$$n(\Delta, \delta) = \sqrt{1 + \chi'}, \qquad \text{or near resonance } (\Delta \approx \delta), \quad n(\Delta) \approx 1 + \frac{1}{2}\chi'.$$

$T(\Delta, \delta)$ and $n(\Delta, \delta)$ are plotted in Figure 7a and 7b, respectively, for coupling field intensities 0.5 mW/cm^2 and 1.0 mW/cm^2.

A3.3. Susceptibility for a Doppler-broadened ensemble

Consider the transmission of a weak probe beam through an Rb vapor cell held at some finite temperature for a coaxial coupling-probe geometry. For a given velocity class v, the probe frequency is shifted to $\Delta + \omega_p v/c$ and the coupling to $\delta + \omega_c v/c$. Since the probe and coupling frequency differ by ~10 ppm, we can assume that $\omega_p = \omega_c$. We integrate $\chi(\Delta)$ (Equation AIII2) over the Maxwell velocity distribution at temperature T

Equation AIII 3

$$n(v)dv = \frac{N}{u\sqrt{\pi}} \mathrm{Exp}\left(-\frac{v^2}{u^2}\right) dv\,, \qquad u = \sqrt{\frac{2k_B T}{m}},$$

and obtain the following expression for χ:

Equation AIII 4

$$\chi = \frac{i\, c\, g^2 {\mu_{21}}^2 N\sqrt{\pi}}{\hbar\, \omega_p\, u\, \epsilon_0} e^{z^2}[1 - \mathrm{erf}(z)],$$

where

$$z = \frac{c}{\omega_p\, u}\left[\gamma - i\Delta + \frac{{\Omega_c}^2}{\gamma_{31} - i(\Delta - \delta)}\right].$$

A3.4. Transmission profile for the probe beam through a RT Rb vapor cell

The above results are derived for a single 3-level system. We shall adapt the model to suit the case of Rb atoms. Rb naturally occurs in ^{85}Rb and ^{87}Rb; ^{87}Rb has fractional abundance $f = 0.2783$ where ^{85}Rb $f = 0.7217$. For a Rb atom there exist hyperfine sub-levels (labeled by F) and within each those degenerate magnetic sub-levels (labeled by m_F). The transitions between pairs of magnetic sub-levels between the ground state (m_F) and the excited state ($m_{F'}$) contribute collectively to the absorption of light. The $m_F \rightarrow m_{F'}$ transitions are governed by selection rules based on the angular momentum of the incident light: for π-polarized light $m_{F'} = m_F$; for σ_+-polarized light $m_{F'} = m_F + 1$; and for σ_--polarized light $m_{F'} = m_F - 1$. The coupling strength g for an $F \rightarrow F'$ transition is given by the square root sum of the individual allowed $m_F \rightarrow m_{F'}$ transition strengths. The coupling strength values are documented in ref [26]. The susceptibility χ is the sum of the contributions from each individual oscillator. At room temperature, the atomic population is approximately evenly distributed among the ground state magnetic sub-levels. Thus for each $m_F \rightarrow m_{F'}$ transition the available population density is $N/[2(2I+1)]$ in the weak probe limit, where I is the nuclear spin and $2(2I+1)$ the total degeneracy of the $5S_{1/2}$ hyperfine levels. The above considerations demands Equation AIII4 to be rewritten as

Equation AIII 5

$$\chi_{FF'}(\Delta, \delta, \Omega_C, T) = \frac{i\, c\, {g_{FF'}}^2 {\mu_{21}}^2 (\mathcal{F}\, N)\sqrt{\pi}}{\hbar\, \omega_p\, u\, \epsilon_0} f \frac{1}{2(2I+1)} e^{{z_{FF'}}^2} [1 - \mathrm{erf}(z_{FF'})],$$

where

$$z_{FF'} = \frac{c}{\omega_p\, u}\left[\gamma - i(\Delta - \xi_{FF'}) + \frac{{\Omega_c}^2}{\gamma_{31} - i(\Delta - \delta)}\right];$$

${g_{FF'}}^2 = \sum {g_{m_F m_{F'}}}^2$ is the square of the total transition strength between F and F'; f is the fractional isotope abundance; and $\xi_{FF'}$ is the frequency difference between the hyperfine resonance and the arbitrarily chosen zero point. A multiplication factor $\mathcal{F}$ is added to the population density N to account for the increase in N in a presence of the strong optical pumping effect from the coupling beam. Note that both N and u are functions of the vapor cell temperature T. The expression for u is given in Equation AIII 3; the expression for N is as follows

Equation AIII 6

$$N = \frac{p}{k_B T} \times \left(133.323\ \frac{\text{Pa}}{\text{Torr}}\right),$$

where the Rb vapor pressure as a function of T in units of Torr is given by [26]:

$$\text{Log}\, p = -94.04826 - \frac{1961.258}{T} - 0.03771687 \times T + 42.57526 \times \text{Log}\, T\,.$$

At room temperature, the hyperfine triplet for each Rb D_2 transition are so closely spaced that their individual Doppler profiles overlap significantly to give a collective, unresolved Doppler profile with FWHM $\sim$530 MHz . The overall transmission profile for each D_2 transition, originating from F, is given by the product of three Doppler profiles, i.e.

Equation AIII 7

$$T_F(\Delta, \delta, \Omega_C, T) = \prod\nolimits_{F'} \text{Exp}\left[-k\ \text{Im}\,\chi_j\, L\right] = \text{Exp}\left[-k\ \left(\sum\nolimits_{F'} \text{Im}\,\chi_j\right) L\right],$$

where $k = \omega_p/c$ is the wave number of the probe beam and L is the length of the sample. Thus, given the probe detuning Δ, the coupling detuning δ, the coupling Rabi frequency Ω_c, and the vapor cell temperature T, the transmission profile can be calculated using Equation AIII 5, Equation AIII6, and Equation AIII7.

References

[1] M. Lu, Ph. D. thesis, University of Nevada, Reno, 2011.

[2] A. Melissinos and J. Napolitano, *Experiments in Modern Physics*, 2nd ed. (Academic Press, NewYork, 1966)

[3] Wineland, D. J., Bergquist, J. C., Itano, W. M., Bollinger, J. J., & Manney, C. H. (1987). Atomic-ion Coulomb clusters in an ion trap. *Physical review letters*, 59(26), 2935.

[4] Boller, K. J., Imamolu, A., & Harris, S. E. (1991). Observation of electromagnetically induced transparency. *Physical Review Letters*, *66*(20), 2593.

[5] Lvovsky, A. I., Sanders, B. C., & Tittel, W. (2009). Optical quantum memory. *Nature Photonics*, *3*(12), 706-714.

[6] Steck, D. A. (2001). Rubidium 87 D line data.

[7] Hawthorn, C. J., Weber, K. P., & Scholten, R. E. (2001). Littrow configuration tunable external cavity diode laser with fixed direction output beam. Review of scientific instruments, 72(12), 4477-4479.

[8] Appel, J., MacRae, A., & Lvovsky, A. I. (2009). A versatile digital GHz phase lock for external cavity diode lasers. *Measurement Science and Technology*, 20(5), 055302.

[9] Wineland, D. J., & Dehmelt, H. G. (1975). Principles of the stored ion calorimeter. *Journal of Applied Physics*, 46(2), 919-930.

[10] Foot, C. J. (1991). Laser cooling and trapping of atoms. *Contemporary Physics*, 32(6), 369-381.

[11] Wieman, C., Flowers, G., & Gilbert, S. (1995). Inexpensive laser cooling and trapping experiment for undergraduate. *Am. J. Phys*, 63(4), 4.

[12] Raab E L, Prentiss M G, Cable A E, Chu S and Pritchard D E (1987) *Phys. Rev. Lett*. 59 2631

[13] K. Luksch, Ph. D. thesis, National University of Singapore, 2012.

[14] Lett, P. D., Watts, R. N., Westbrook, C. I., Phillips, W. D., Gould, P. L., & Metcalf, H. J. (1988). Observation of atoms laser cooled below the Doppler limit. *Physical Review Letters*, 61(2), 169-172.

[15] Brzozowski, T. M., Maczynska, M., Zawada, M., Zachorowski, J., & Gawlik, W. (2002). Time-of-flight measurement of the temperature of cold atoms for short trap-probe beam distances. *Journal of Optics B: Quantum and Semiclassical Optics*, 4(1), 62.

[16] Tiwari, V. B., Singh, S., Rawat, H. S., Singh, M. P., & Mehendale, S. C. (2010). Electromagnetically induced transparency in cold 85Rb atoms trapped in the ground hyperfine F= 2 state. *Journal of Physics B: Atomic, Molecular and Optical Physics*, 43(9), 095503.

[17] Mayer, S., & Olson, A. (2008). Electromagnetically induced transparency in rubidium: An advanced undergraduate laboratory. *Bulletin of the American Physical Society*, 53.

[18] Hopkins, S. A., Usadi, E., Chen, H. X., & Durrant, A. V. (1997). Electromagnetically induced transparency of laser-cooled rubidium atoms in three-level Λ-type systems. *Optics communications*, 138(1), 185-192.

[19] Feng, X., Rui-Min, G., Shuai, C., Yu, Z., Lu-Ming, L., & Xu-Zong, C. (2003). Observation of electromagnetically induced transparency in a Zeeman-sublevel system in rubidium atomic vapour. *Chinese physics letters*, 20(8), 1257.

[20] Fowles, G. R. (1968). Introduction to modern optics. New York: Holt, Rinehart and Winston.

[21] Phillips, D. F., Fleischhauer, A., Mair, A., Walsworth, R. L., & Lukin, M. D. (2001). Storage of light in atomic vapor. *Physical Review Letters*, *86*(5), 783.

[22] Dudin, Y. O., Li, L., & Kuzmich, A. (2013). Light storage on the time scale of a minute. *Physical Review A*, *87*(3), 031801.

[23] Lukin, M. D. (2003). Colloquium: Trapping and manipulating photon states in atomic ensembles. *Reviews of Modern Physics*, 75(2), 457.

[24] Höckel, D., Scholz, M., & Benson, O. (2009). A robust phase-locked diode laser system for EIT experiments in cesium. *Applied Physics B*, 94(3), 429-435.

[25] Li, Y. Q., & Xiao, M. (1995). Electromagnetically induced transparency in a three-level Λ-type system in rubidium atoms. *Physical Review A*, 51(4), R2703.

[26] Siddons, P., Adams, C. S., Ge, C., & Hughes, I. G. (2008). Absolute absorption on rubidium D lines: comparison between theory and experiment. *Journal of Physics B: Atomic, Molecular and Optical Physics*, 41(15), 155004.

[27] Scully, M. O. (1997). *Quantum optics*. Cambridge university press. Chicago